Section 5

Development of and studies with regional and convective-scale atmospheric models and ensembles.

Hourly updated NOAA 3km High-Resolution Rapid Refresh model

Curtis Alexander, Stan Benjamin, David Dowell, Stephen Weygandt, John Brown, Joseph Olson, Tatiana Smirnova, Jaymes Kenyon, Terra Ladwig, Isidora Jankov

NOAA Earth System Research Laboratory, Boulder, Colorado USA. Curtis.alexander@noaa.gov

The time scale or lifetime of many weather phenomena can be from around 1 h (rotating convective storms) down to several minutes or less (e.g., individual clouds, eddies, etc.), a motivation for rapid updating NWP using recent observations to represent the current situation in the model state for these phenomena. The NOAA 3km High-Resolution Rapid Refresh (HRRR) now assimilates radar every 15 min. Data assimilation and model configuration in the HRRR has been refined over the past few years for all-season boundary-layer forecasting including clouds, precipitation, and convective environment. The HRRR model is described in Benjamin et al 2016 (B16). HRRR forecast skill for radar reflectivity has continued to improve consistently each year through 2015 (Fig. 2).

RAPv4/HRRRv3 Summary of Changes – Feb 2018

Implementation RAPv4/HRRRv3

Larger RAP Domain

Model	Run at:	Domain	Grid Points	Grid Spacing	Vertical Levels	Pressure Top	Boundary Conditions	Initialized
RAP	GSD, NCEP	North America	953 x 834	13 km	50	10 hPa	GFS	Hourly (cycled)
HRRR	GSD, NCEP	CONUS	1799 x 1059	3 km	50	20 hPa	RAP	Hourly (pre-forecast hour cycle)

Newer Model Version
More Ensemble Weight
Advanced Physics

Model	Version	Assimilation	Radar DA	Radiation LW/SW	Microphysics	Cumulus Param	PBL	LSM
RAP	WRF-ARW v3.9 - hyb	GSI Hybrid Ens to 0.85, better cld	13-km 3dLH-DFI	RRTMG/ RRTMG	Thompson Aerosol v3.9	GF + Shallow	MYNN v3.9	RUC v3.9
HRRR	WRF-ARW v3.9 - hyb	GSI Hybrid Ens to 0.85, better cld	3-km 15-min LH	RRTMG/ RRTMG	Thompson Aerosol v3.9	None	MYNN v3.9	RUC v3.9

Seasonal Vegetation Fraction/Leaf Area Index

Model	Horiz/Vert Advection	Scalar Advection	Upper-Level Damping	6th Order Diffusion	SW Radiation Update	Land Use	MP Tend Limit	Time-Step
RAP	5th/5th	Positive-Definite	w-Rayleigh 0.2	Yes 0.12	20 min	15" MODIS Seasonal	0.01 K/s	60 s
HRRR	5th/5th	Positive-Definite	w-Rayleigh 0.2	Yes -0.25 (slope dep)	15 min with SW-dt	15" MODIS Seasonal	0.07 K/s	20 s

11

Fig 1. Characteristics including physical parameterizations for 3km HRRRv3 and RAPv4, expected for implementation at NCEP in February 2018. Key changes from HRRRv2/RAPv3 are shaded in red.

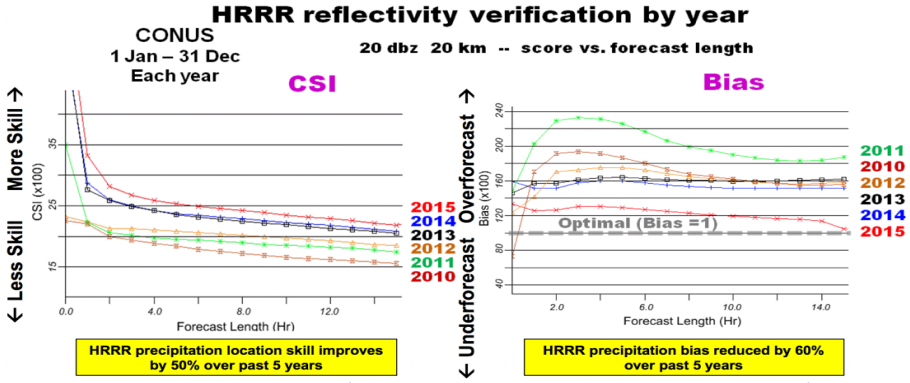

Fig 2. Radar reflectivity verification (Critical Success Index on left, bias on right) for 3km HRRR model for 2010-2015. HRRR and radar observations are averaged at 20km scale and threshold is 20 dBZ reflectivity.

The HRRR and RAP models were recently updated (HRRRv2/RAPv3) at NOAA/NCEP in August 2016. An overall description of the RAPv3/HRRRv2 configuration for model and assimilation details are described in B16.

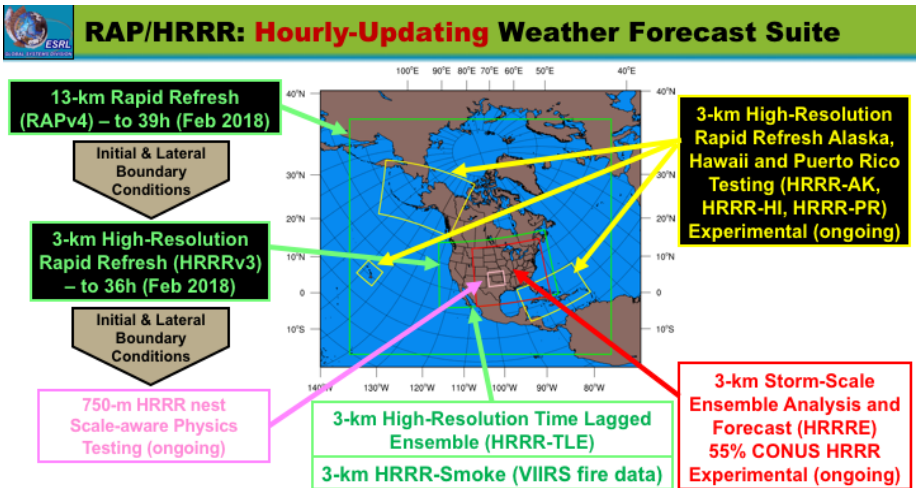

Fig 3. Experimental versions of High-Resolution Rapid Refresh (HRRR) running at NOAA Earth System Research Lab, with Feb 2018 upgrade of operational version of HRRR model at NCEP.

In 2017, a HRRR Ensemble was tested and evaluated with a 40-member 3km ensemble for data assimilation showing for 1-7h duration improved reflectivity (Fig. 4) vs. the HRRR with non-3km-ensemble data assimilation. Improved versions of the HRRR Ensemble will be tested in 2018. A description of the HRRR Ensemble (version 2017) is provided in Figure 5, including hourly assimilation with 36 members running at 3km. Ensemble forecasts were run with 9 members every 3 hours.

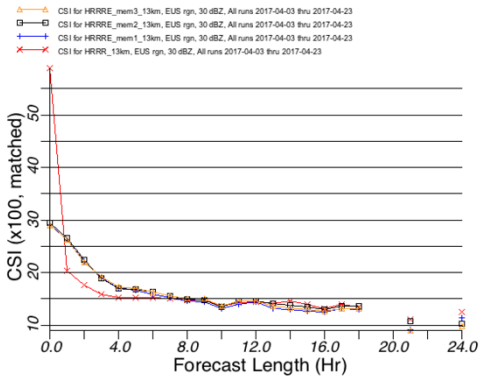

Fig 4. Radar reflectivity Critical Success Index verification for deterministic HRRR (red) and 3 members of the HRRR Ensemble. 2018 upgrade of operational version of HRRR

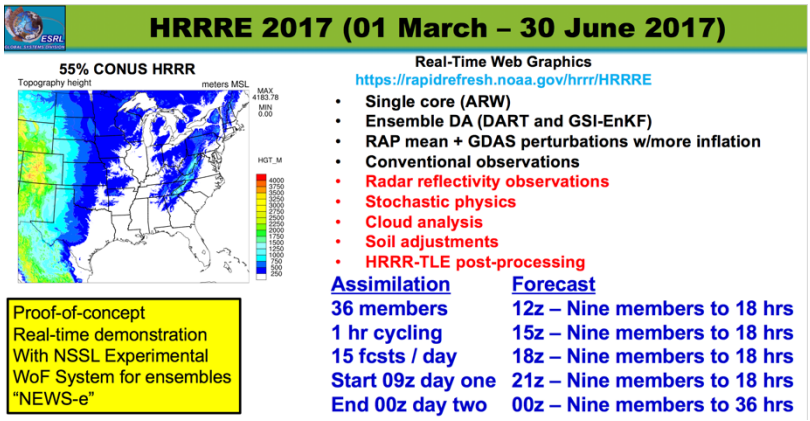

Fig 5. Description of the experimental 2017 HRRR Ensemble data assimilation and model system run by NOAA Earth System Research Laboratory.

Benjamin, S.G., S.S. Weygandt, M. Hu, C.A. Alexander, T.G. Smirnova, J.B. Olson, J.M. Brown, E. James, D.C. Dowell, G.A. Grell, H. Lin, S.E. Peckham, T.L. Smith, W.R. Moninger, G.S. Manikin, **2016**, A North American hourly assimilation and model forecast cycle: The Rapid Refresh. *Mon. Wea. Rev.*, **144**, 1669-1694. http://dx.doi.org/10.1175/MWR-D-15-0242.1

Experiments with stochastic perturbation of physical tendencies in the mesoscale convection-resolving ensemble COSMO-Ru2-EPS

Dmitry Alferov and Elena Astakhova

Hydrometcenter of Russia

11-13, B. Predtechensky per., Moscow, 123242, Russia

dalferov@mecom.ru, elena_ast_hmc@mail.ru

Introduction

Insufficient ensemble spread is a well-known problem in ensemble forecasting. Various methods have been developed to account for model-related uncertainty in global and regional ensemble prediction systems (EPS) which benefit from their usage. The applicability and efficiency of these methods for convective-resolving EPSs are under research. This paper analyses how the introduction of stochastic perturbations of physical tendencies (SPPT scheme) [1] affects the spread and performance of a convective-resolving EPS based on COSMO model.

Experiment setup

In our experiments, we used the COSMO-Ru2-EPS system with a 2.2 km resolution that had been previously developed within the framework of the COSMO Priority project CORSO [6] and WWRP FDP/RDP FROST-2014 [2] for the Sochi region. The system provided a dynamical downscaling of COSMO-S14-EPS, the 7-km Italian ensemble prediction system for the Sochi-2014 Olympics. In turn, COSMO-S14-EPS was a clone of COSMO-LEPS [3] moved to the Sochi region. The systems are described in detail in [4, 5]. Both COSMO-S14-EPS and COSMO-Ru2-EPS ran operationally during the Olympic Games 2014 providing probabilistic products to Sochi forecasters. The ensemble size was 10 in both systems. SPPT scheme was not included. The operational COSMO-Ru2-EPS forecasts for February 2014 starting at 00 and 12 UTC were used as a reference in the study.

SPPT scheme was adapted to the COSMO model by Lucio Torrisi and introduced to the official COSMO code in 2014 [7]. To test the SPPT scheme and to assess its effect on the forecast spread and skill, numerical experiments were carried out with COSMO-Ru2-EPS for the same period, initial and boundary conditions as operational forecasts of 2014. Additionally, sensitivity to SPPT parameters, governing the perturbation size and spatiotemporal correlations, as well as to the selection of various humidity perturbations, was examined.

Both case studies and verification of monthly series of forecasts were carried out.

Results and conclusions

Case studies demonstrated that SPPT could be useful for precipitation forecasts improving the description of the rain location and start. The analysis of T_{2m} predictions in the tropospheric Foehn case (February 7, 2014) revealed the correlation between the T_{2m} ensemble spread and the model orography (see Fig.1). Also the coincidence between high-spread areas and the areas of less skillful forecast was found.

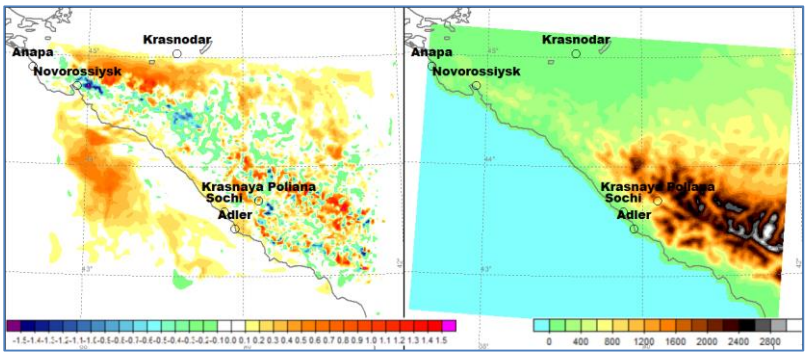

Fig.1. The difference between the T_{2m} ensemble spread in experiments with and without SPPT (left) and the COSMO model orography (right).

30h forecast starting at 00UTC on February 6, 2014.

For probabilistic verification, the Brier score, the Brier skill score and the area under the ROC curve were calculated for the monthly series of COSMO-Ru2-EPS forecasts (56 in total).

Some positive effect of using SPPT was found for precipitation forecasts, especially for the event "3-h precipitation is greater than 1 mm". Variations in the SPPT parameters did not influence the results much.

SPPT does not improve the skill of 2-m temperature forecasts. At the same time, the eyeball analysis shows that introduction of SPPT makes the predicted T_{2m} distribution more realistic. This is supported by comparing the distribution histograms for forecasts with and without SPPT and observations (Fig. 2). Thus, SPPT did not add value to temperature forecasts, but can sometimes improve the representation of its distribution.

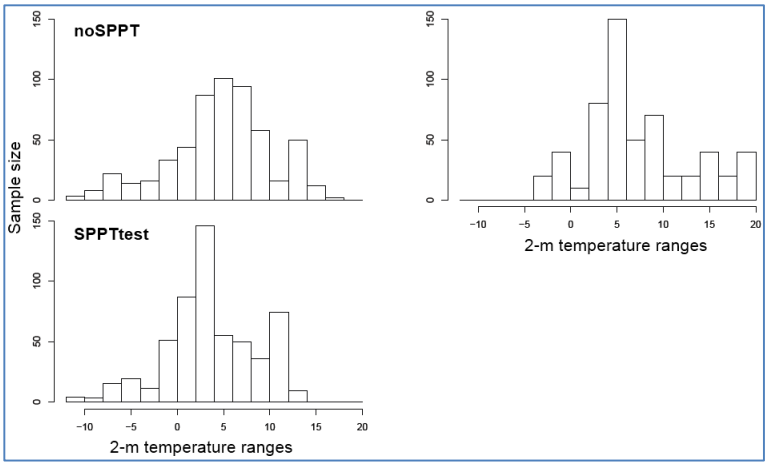

Fig.2. 2-m temperature distribution histograms for 48-h forecasts with and without SPPT (left) and for observations (right). February 2014.

At the same time, the verification scores for 2-m temperature forecasts showed rather large sensitivity to variation of SPPT parameters. It was found that the 2-m temperature forecasts can be improved by adjusting the SPPT parameters. For example, perturbing all hydrometeor tendencies in most cases leads to better results than perturbing only specific water content tendency. Increasing the range of standard deviation for the Gaussian distribution of random numbers and using the higher upper limit imposed to the absolute value of random numbers also positively contributed to the results.

Acknowledgments

The authors are grateful to Anatoly Muravev for verification software and to Andrea Montani for providing initial and boundary conditions. The study was made within the COTEKINO and SPRED COSMO priority projects.

References

1. R. Buizza, M. Miller, and T. Palmer, 1999: Stochastic representation of model uncertainties in the ECMWF Ensemble Prediction System. *Q. J. R. Met. Soc.*, vol. 125, P. 2887–2908.
2. Kiktev, D., P. Joe, G. Isaac, A. Montani, I. Frogner, P. Nurmi, B. Bica, J. Milbrandt, M. Tsyrulnikov, E. Astakhova, A. Bundel, S. Belair, M. Pyle, A. Muravyev, G. Rivin, I. Rozinkina, T. Paccagnella, Y. Wang, J. Reid, T. Nipen, and K. Ahn, 2017: FROST-2014: The Sochi Winter Olympics International Project. *Bull. Amer. Meteor. Soc.* DOI:10.1175/BAMS-D-15-00307.1, in press.
3. A. Montani, D. Cesari, C. Marsigli, and T. Paccagnella, 2011: Seven years of activity in the field of mesoscale ensemble forecasting by the COSMO-LEPS system: main achievements and open challenges. *Tellus*, 63A, 605-624. DOI: 10.1111/j.1600-0870.2010.00499.x
4. A. Montani, C. Marsigli, and T. Paccagnella, 2013: Development of a COSMO-based limited-area ensemble system for the 2014 Winter Olympic Games. *COSMO Newsletter*, No. 13, 93–99. Available online at http://cosmo-model.org/content/model/documentation/newsLetters/newsLetter13/cnl13_12.pdf.
5. A. Montani, D. Alferov, E. Astakhova, C. Marsigli, and T. Paccagnella, 2014: Ensemble forecasting for Sochi-2014 Olympics: the COSMO-based ensemble prediction systems. *COSMO Newsletter*, No. 14, 88–94. Available online at http://cosmo-model.org/content/model/documentation/newsLetters/newsLetter14/cnl14_10.pdf.
6. G. Rivin and I. Rozinkina, 2011: Priority Project "CORSO": Consolidation of Operation and Research results for the Sochi Olympic Games. Available online at http://cosmo-model.org/content/tasks/pastProjects/corso/default.htm.
7. U. Schaettler, G. Doms, and C. A. Schraff, 2014: Description of the Nonhydrostatic Regional COSMO-Model. Part VII: User's Guide. Offenbach. November 2014. 211 p.

Numerical prediction experiment over the United Arab Emirates by using JMA-NHM

Akihiro Hashimoto[1], Narihiro Orikasa[1], Takuya Tajiri[1] and Masataka Murakami[2,1]

[1]*Meteorological Research Institute, Japan Meteorological Agency, Tsukuba, Japan*
[2]*Institute for Space-Earth Environmental Research, Nagoya University, Nagoya, Japan*

1. Introduction

In 2015, the United Arab Emirates (UAE) Research Program (UAEREP) for Rain Enhancement Science was launched in order to promote scientific advancement and development of new technology. Three projects among many proposed projects were awarded the UAEREP prize. The authors are involved in one of these three projects, "Advanced Study on Precipitation Enhancement in Arid and Semi-Arid Regions," which has four subprojects; (1) data analysis for identifying areas suitable for cloud seeding, (2) laboratory experiments for characterization of seeding material, (3) ground-based observation for evaluating the occurrence frequency of seedable clouds and an airborne seeding experiment for investigating seeding effects in clouds, and (4) numerical modeling for realistic simulation of cloud seeding and the seasonal evaluation of seeding effect. As a collaborative work among subprojects, daily numerical weather prediction over the UAE began in late 2016 to support safe and effective experiments of airborne cloud seeding and to evaluate model performance. This article presents a description of the prediction system and its preliminary results.

2. Numerical prediction system

The numerical prediction system was established based on the Japan Meteorological Agency's Non-Hydrostatic Model (JMA-NHM, Saito *et al*., 2006) with several modifications, mainly land surface configuration, as described in Hashimoto et al. (2017).

The numerical prediction is conducted twice per day. In each prediction cycle, the simulation with a 5-km horizontal resolution (5km-NHM) is performed first, followed by that with a 1-km horizontal resolution (1km-NHM). Figure 1 shows the computational domain. The 5km-NHM widely, but not completely, covers the Middle East including arid and semi-arid regions in the UAE. The 1km-NHM is embedded in the domain of 5km-NHM. The standard latitude and longitude are at 20.00 ºN and 55.00 ºE, respectively, in the Lambert conformal conic projection. The center of the domain is located at (24.00 ºN, 54.00 ºE) for the 5km-NHM, and at (24.25 ºN, 54.15 ºE) for the 1km-NHM. In the vertical direction, the two simulations are configured identically as follows. The top height of the model domain is 22 km. The vertical grid spacing stretches from 40 m at the surface to 886 m at the top of the domain. Fifty vertical layers are employed in a terrain-following coordinate system.

The initial time of the 5km-NHM forecast is 0400 or 1600 Gulf Standard Time (GST=UTC+4), which corresponds to the forecast time FT = 6 h of the JMA's Global Spectral Model (GSM) forecast with initial times of 2200 or 1000 GST, respectively. The initial time of the 1km-NHM forecast is shifted 12 h later from that of the 5km-NHM forecast. Boundary conditions are provided by the JMA's GSM forecast every 6 h. The 1km-NHM is driven by the hourly meteorological field of the 5km-NHM forecast in the one-way nesting manner. Figure 2 shows the schedule and data flow in the numerical prediction system with the initial time of 0400 GST, for instance. The integration time and time step are 48 h and 12 s for the 5km-NHM, and 27 h and 8 sec for the 1km-NHM, respectively. Hourly output is obtained from each simulation.

Corresponding author: Akihiro Hashimoto, Meteorological Research Institute, 1-1 Nagamine, Tsukuba, 305-0052, Japan. E-mail: ahashimo@mri-jma.go.jp

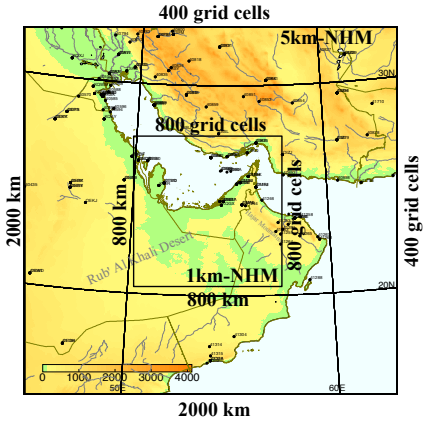

Fig. 1. Computational domain for the numerical prediction.

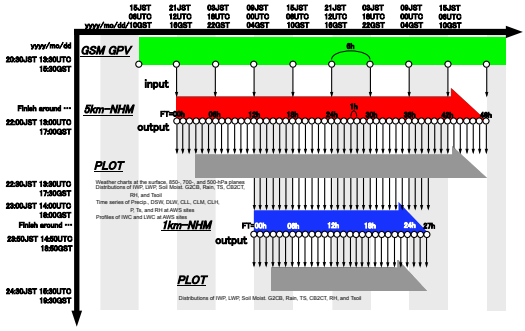

Fig. 2. Schedule for the weather prediction with the initial time of 0400 GST. Fine black arrows indicate the data flow.

3. Computational cost

Computations are conducted on the FUJITSU Supercomputer PRIMEHPC FX100 at the Meteorological Research Institute (MRI) of the JMA. Each job runs with 128 Multi Processor Interface (MPI, 8 MPI x 16 nodes) for the 5km-NHM simulation twice per day, which finishes in about one and a half hours. This costs 17,520 node-hours for year-round simulations (16 nodes x 1.5 h x 2 runs x 365 days). Maximum memory usage is about 10 GB/node. For the 1km-NHM simulation, each job runs with 288 MPI (8 MPI x 36 nodes) twice per day, which also finishes in about one and a half hours. This costs 39,420 node-hours for year-round simulations (36 nodes x 1.5 h x 2 runs x 365 days). Maximum memory usage is about 25 GB/node.

A single run of 5km-NHM requires 20.3 GB of free disk space

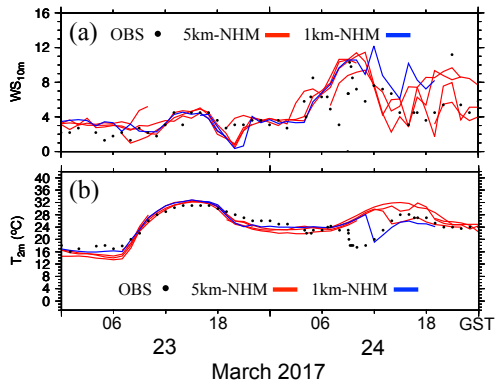

Fig. 3 Observed and predicted results for (a) surface wind speed and (b) surface air temperature at Al Ain International Airport. Black dot indicates the observation. Red and blue lines indicate the 5km- and 1km-NHM predictions, respectively.

for input/output operation. We are archiving two-dimensional data, vertical profiles above observation sites, and plotted graphs for each simulation. The size of the archived data is 1.5 GB/run. This needs the storage space of 949 GB/year. For the 1km-NHM, 84.4 GB/run and 1,678 GB/year are required for running a job and archiving the data, respectively.

4. Result

Figure 3 shows the observed and predicted results for surface wind speed and surface air temperature on 23 and 24 March 2017 at Al Ain International Airport, which will be the base of our airborne cloud seeding experiments planned in the summer of 2017. The 5km- and 1km-NHM predicted well the variation of surface wind speed and air temperature on 23 March. In the morning on 24 March, when a synoptic scale disturbance accompanied with precipitation passed over the observation site, a temperature drop of 6 ºC was observed. This temperature drop was predicted within a delay of a few hours by the 1km-NHM simulation with an initial time of 1200 UTC on 23 March as compared to the actual event. For the 5km-NHM, we have three forecast results available for this temperature drop event with different initial times; 0000, 1200 and 2400 UTC on 23 March. The best result was obtained from the forecast with an initial time of 0000 UTC on 23 March, although the forecast shows a larger delay time and a smaller magnitude of temperature drop than the observation and the 1km-NHM forecast. Figures 4a and 4b show time-height cross-sections of air temperature at Al Ain International Airport observed by multi-wavelength microwave radiometer (MP-3000, Radiometrics) and predicted by the 1km-NHM, respectively. Air temperature below a height of 2-km began to decrease several hours earlier (Fig. 4a) than the surface air temperature drop (Fig. 3b). The predicted temperature decrease at the lower layer preceding the surface air temperature drop (Fig. 4b) was much weaker than the observed decrease (Fig. 4a). K-band Doppler radar (MRR-2, METEK), which was deployed at the same site, detected precipitation during the preceding decrease in low-level air temperature (Fig. 4c), while, in the prediction, the precipitation does not appear until just before the temperature drop (Fig. 4d). This indicates that the cooling of low-level air due to evaporation of precipitation particles was not represented very well in the prediction. To improve the prediction accuracy, it is necessary to consider the predictability of synoptic scale disturbances as well as thermo-dynamical formulations of the prediction system.

5. Summary

A numerical prediction system was established based on the JMA-NHM to support airborne cloud seeding experiments and to evaluate model performance. The procedure of the numerical prediction was described including the computational resources required for performing numerical simulations and for archiving the simulation results. Preliminary results of a comparison between ground-based observation and numerical prediction were presented with respect to the event of surface air temperature drop on 24 March 2017 at Al Ain International Airport. More validation and improvement of the model will be the subject of future study.

Acknowledgement

This study was conducted as a part of the project "Advanced Study on Precipitation Enhancement in Arid and Semi-Arid Regions" that is supported by the UAEREP for Rain Enhancement Science, an initiative of the Ministry of Presidential Affairs, under the management of the National Center of Meteorology and Seismology.

References

Hashimoto, A., M. Murakami and S. Haginoya, 2017: First application of JMA-NHM to meteorological simulation over the United Arab Emirates. SOLA, submitted.

Saito, K., T. Fujita, Y. Yamada, J. Ishida, Y. Kumagai, K. Aranami, S. Ohmori, R. Nagasawa, S. Kumagai, C. Muroi, T. Kato, H. Eito, Y. Yamazaki, 2006: The operational JMA nonhydrostatic mesoscale model. *Mon. Wea. Rev.*, **134**, 1266–1298.

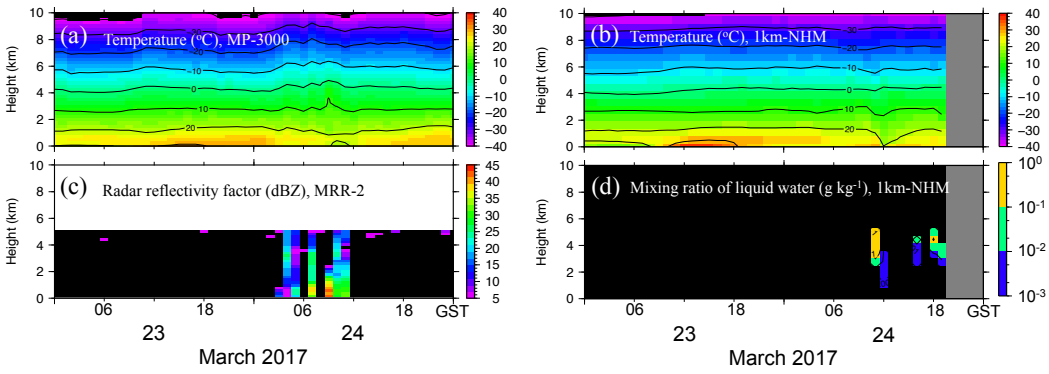

Fig. 4 Time-height cross sections of temperature (a) observed by multi-wavelength microwave radiometer and (b) predicted by the 1km-NHM, (c) reflectivity factor observed by micro-rain radar and (d) mixing ratio of liquid water predicted by the 1km-NHM.

Prediction of Antarctic weather by JMA-NHM to support JARE

Akihiro Hashimoto[1], Kyohei Yamada[2], Naohiko Hirasawa[2], Masashi Niwano[1] and Teruo Aoki [3,1]

[1]*Meteorological Research Institute, Japan Meteorological Agency, Tsukuba, Japan*
[2] *Polar Meteorology and Glaciology Group, National Institute of Polar Research, Tachikawa, Japan*
[3]*Graduate School of Natural Science and Technology, Okayama University, Okayama, Japan*

1. Introduction

The 6-year phase IX of the Japanese Antarctic Research Project began in the 2016–17 austral summer with the main scientific theme of "Investigation of changes in the Earth system from Antarctica". This project uses the Japan Meteorological Agency's Non-Hydrostatic Model (JMA-NHM; Saito *et al*., 2006) for weather prediction over the entire Antarctic continent to support the activities of the Japanese Antarctic Research Expedition (JARE). This article describes the numerical prediction system and preliminary results.

2. Numerical prediction system

The numerical prediction system is established based on the JMA-NHM with several modifications, as described in Hashimoto et al. (2016, 2017), to better represent the meteorological processes over the ice sheet, since the original model was fitted to mid-latitude environments.

The computational domain is 6096 km × 5664 km wide and its horizontal resolution is 6 km (1016 x 944 grid cells). The standard latitude and longitude are at 80.00 °S and the prime meridian, respectively, in the polar stereographic projection. The lower left point of the domain is located at 54.63 °S, 132.47 °W (Fig. 1). The top height of the domain is 22 km. There are 50 layers in the vertical direction, increasing from 40 m thick at the surface to 886 m at the top in a terrain-following coordinate system. The integration time is 42 h, with a timestep of 15 s. The radiative process are computed every 15 min at a horizontal grid spacing of 12 km. The initial and boundary conditions are obtained from the JMA's global forecast. The model topography is based on the 5-km-mesh surface elevation data from the digital elevation model of Antarctica provided by Le Brocq et al. (2010).

The simulation is performed twice a day starting at 0900 or 2100 SYOT (UTC+3), corresponding to the forecast time FT = 6 h in the JMA's global forecast starting at 0300 or 1500 SYOT, respectively. Boundary conditions are given every 6 h. Figure 2 shows the schedule and data flow for the prediction starting at 0900 SYOT.

Computations are run on the HITACHI SR24000 Model XP1 supercomputer at the National Institute of Polar Research (NIPR).

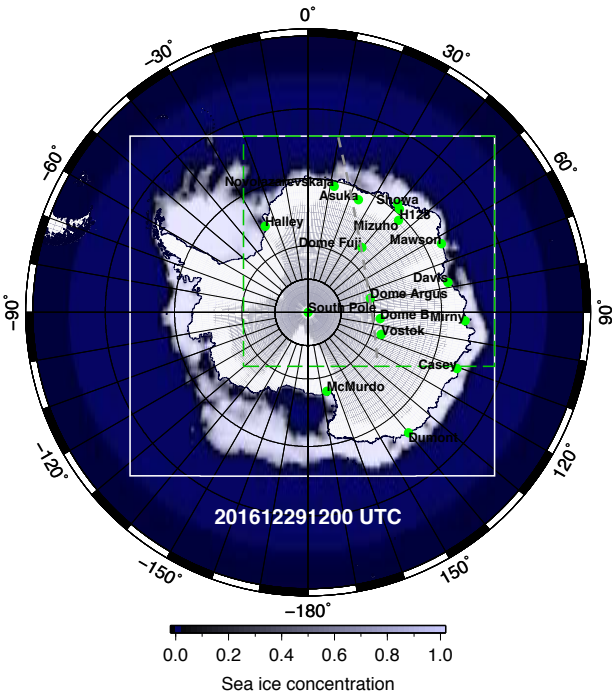

Fig. 1. Computational domains of the weather model (white line) and the test-bed system (green broken line). The gray broken line shows the CloudSat orbit corresponding to Fig. 5.

Corresponding author: Akihiro Hashimoto, Meteorological Research Institute, 1-1 Nagamine, Tsukuba, 305-0052, Japan. E-mail: ahashimo@mri-jma.go.jp

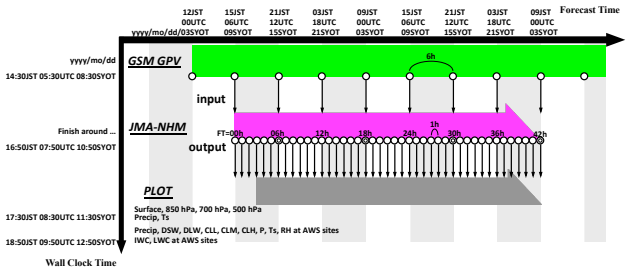

Fig. 2. Schedule of weather prediction starting at 0900 SYOT. Fine black arrows indicate data flow.

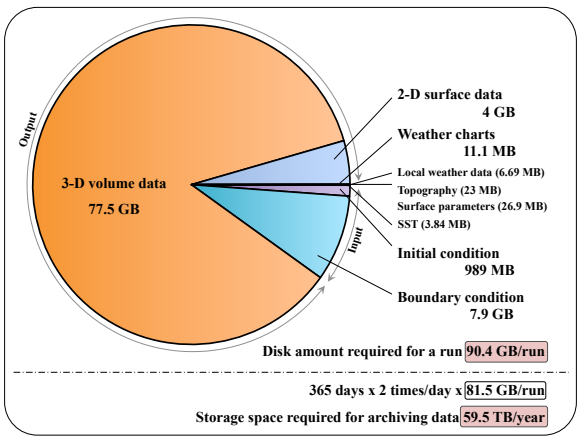

Fig. 3 Data storage required for one run of the weather prediction model and for archiving data for a year.

Each job runs with 320 Multi Processor Interface (MPI, 20 MPI x 16 nodes) and finishes in about 2 h. This costs 23,360 node-hours/year (16 nodes x 2 h x 2 runs x 365 days). Each run needs 90.4 GB of free disk space for input/output operation (Fig. 3). For archiving the data, including vertical profiles above observation sites and plotted graphs for each simulation, the data size is 81.5 GB/run, which equals to 59.5 TB/year. Excluding the three-dimensional from the archive reduces this to 4.0 TB/year. A test-bed system is also operated once a day with a smaller domain (Fig. 1) at the Meteorological Research Institute in parallel with the main system as a backup and for testing for improvement of the system in future. In the next section, we present preliminary results from the test-bed system.

3. Preliminary results from test-bed system

Figure 4 shows the observed and predicted results for surface wind speed and surface air temperature from 22 December 2016 to 15 February 2017. Wind speeds of >10 m s^{-1} were observed in several storm events accompanied by synoptic-scale perturbations (Fig. 4a). The model predicted these winds well. On the other hand, in the absence of considerable synoptic scale forcing, during the first couple of weeks, the model over-predicted the wind speed, which was mostly < 2 m s^{-1}. The model tended to underestimate surface air temperature throughout most of the period (Fig. 4b). Local air circulation near Syowa station is likely to be influenced by coastal topography. These results indicate that it is difficult for a model with a horizontal resolution of several kilometers to precisely predict the transport of heat and momentum by local circulation. Figure 5 shows reflectivity at 1400 on 29 December 2016 observed by CloudSat Cloud Profiling Radar (CPR) and simulated by the Joint-Simulator (Hashino et al. 2013) from the output from the JMA-NHM. Both observations and the model consistently detected cloud systems over the Antarctic Ocean and over the slope of the Antarctic ice sheet.

4. Summary

A numerical weather prediction system was established based on the JMA-NHM to support the activities of JARE in Antarctica and for performance evaluation. Comparisons between observations and model predictions of local weather at Syowa station and vertical cross-sections of cloud systems agreed well. Further validation and improvement of the model will be the basis of future work.

Acknowledgement

This study is part of the Science Program of the Japanese Antarctic Research Expedition (JARE). It was supported by National Institute of Polar Research (NIPR) under the Ministry of Education, Culture, Sports, Science and Technology (MEXT).

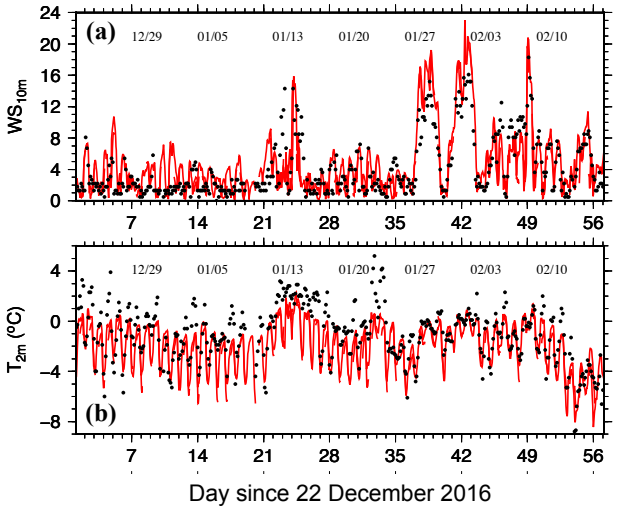

Fig. 4 Observed and predicted (a) surface wind speed and (b) surface air temperature.

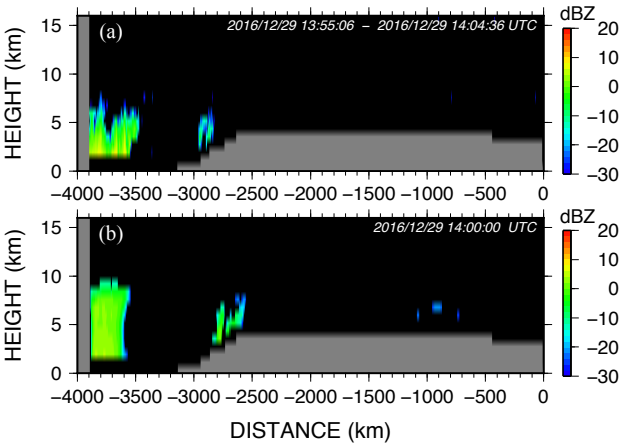

Fig. 5 Cloud reflectivity (a) observed by CloudSat Cloud Profiling Radar on 29 December 2016 along the orbit shown in Fig. 1 and (b) simulated by Joint Simulator from output from the JMA-NHM.

References

Hashimoto, A., M. Niwano, and T. Aoki, 2016: Numerical weather prediction supporting cryospheric field observation campaign on the Greenland Ice Sheet. *J. Japan. Soc. Snow Ice (Seppyo)* **78**, 205-214. (in Japanese with English abstract and captions)

Hashimoto, A., M. Niwano, T. Aoki, S. Tsutaki, S. Sugiyama, T. Yamasaki, Y. Iizuka, and S. Matoba, 2017: Numerical weather prediction system based on JMA-NHM for field observation campaigns on the Greenland ice sheet. *Low Tem. Sci.*, **75**, 91-104, doi:10.14943/lowtemsci.75.91.

Hashino, T., M. Satoh, Y. Hagihara, T. Kubota, T. Matsui, T. Nasuno, and H. Okamoto (2013), Evaluating cloud microphysics from NICAM against CloudSat and CALIPSO, *J. Geophys. Res.*, 118, 7273-7292, doi:10.1002/jgrd.50564.

Le Brocq, A. M., A. J. Payne, and A. Vieli, 2010: An improved Antarctic dataset for high resolution numerical ice sheet models (ALBMAP v1). *Earth System Science Data*, **2**, 247-260. doi: 10.5194/essd-2-247-2010.

Saito, K., T. Fujita, Y. Yamada, J. Ishida, Y. Kumagai, K. Aranami, S. Ohmori, R. Nagasawa, S. Kumagai, C. Muroi, T. Kato, H. Eito, and Y. Yamazaki, 2006: The operational JMA nonhydrostatic mesoscale model. *Mon. Wea. Rev.*, **134**, 1266–1298.

Numerical weather prediction experiment in collaboration with research activities in glaciology and snow disaster prevention

Akihiro Hashimoto[1], Masashi Niwano[1], Teruo Aoki[2,1], Hiroki Motoyoshi[3], Satoru Yamaguchi[3] and Sento Nakai[3]

[1]*Meteorological Research Institute, Japan Meteorological Agency, Tsukuba, Japan*
[2]*Graduate School of Natural Science and Technology, Okayama University, Okayama, Japan*
[3]*Snow and Ice Research Center, National Research Institute for Earth Science and Disaster Resilience, Nagaoka, Japan*

1. Introduction

Falling snow has a large effect on water and heat transport in the atmosphere through gravitational sedimentation and diabatic processes. It also considerably affects civic life and economic activities through its accumulation on the ground. Snowpack conditions directly determine the temporal and spatial distribution of snow cover, the run-off of meltwater into river basins, snow loading on roofs, the occurrence of avalanches, and other factors. In tern, snowpack conditions are closely related to the meteorological factors such as the type of snow particles, air temperature, wind speed, and so on. However, our understanding of the link between falling and fallen snow is still insufficient for precisely predicting the state of the snowpack from meteorological conditions.

A numerical weather prediction experiment began in the winter of 2015 for the purpose of promoting the research activities across the meteorological and glaciological research field. This article describes the numerical weather prediction system, and the preliminary results of a case study for an avalanche which recently occurred close to a ski resort in Japan.

2. Numerical prediction system

The numerical prediction system was established based on the Japan Meteorological Agency's Non-Hydrostatic Model (JMA-NHM, Saito *et al*., 2006) with the option of a double-moment bulk cloud microphysics scheme to predict both the mixing ratio and concentration of particles of solid hydrometeors (i.e., cloud ice, snow, and graupel) and a single-moment scheme to predict only the mixing ratio of particles of liquid hydrometeors (i.e., cloud water and rain).

The numerical prediction is conducted twice per day. Each time, a simulation is first performed with a 5-km horizontal resolution (5km-NHM) in a 2250 km × 2250 km (450 x 450 grid squares) wide domain (Domain1 in Fig. 1). Next, two simulations with a 1-km horizontal resolution (1km-NHM-D2 and -D3) are performed in different domains embedded within Domain1 (Domain2 and 3 in Fig.1). For all three simulations, the standard latitude and longitude are at 60.00 ^{o}N and 140.00 ^{o}E, respectively, in the Lambert conformal conic projection. The center of the domain is located at (39.00 ^{o}N, 137.00 ^{o}E) for the 5km-NHM, and at (43.50 ^{o}N, 142.20 ^{o}E) and (37.00 ^{o}N, 139.00 ^{o}E) for the 1km-NHM-D2 and –D3, respectively.

For the 5km-NHM, the top height of the model domain is 22 km. Vertical grid spacing is stretched from 40 m at the surface to 886 m at the top of the domain. Fifty vertical layers in a terrain-following coordinate system are employed. The integration time is 45 h, with a timestep of 15 s. Computations of the radiative process are performed every 15 min at a horizontal grid spacing of 10 km. The initial and boundary conditions are obtained from the JMA's regional forecast by Meso-Scale Model (MSM). The initial time is 0000 or 1200 JST (UTC+9). The boundary condition is provided every 3 h. Figure 2 shows the schedule and data flow in the numerical prediction with the initial time of 1200 JST, as an example

Corresponding author: Akihiro Hashimoto, Meteorological Research Institute, 1-1 Nagamine, Tsukuba, 305-0052, Japan. E-mail: ahashimo@mri-jma.go.jp

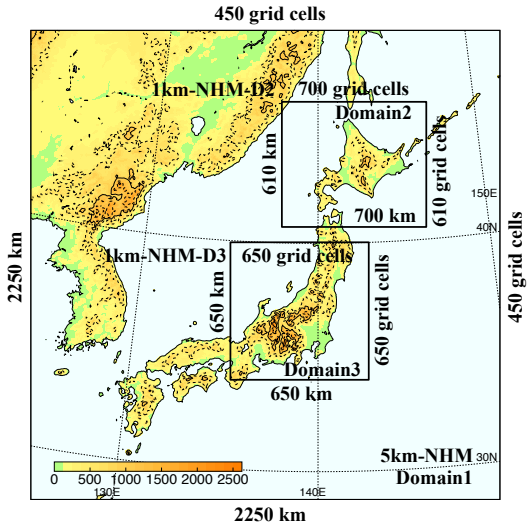

Fig. 1. Computational domains for the numerical prediction. Domain1 is for the 5km-NHM. Domain2 and Domain 3 are for the 1km-NHM-D2 and -D3, respectively.

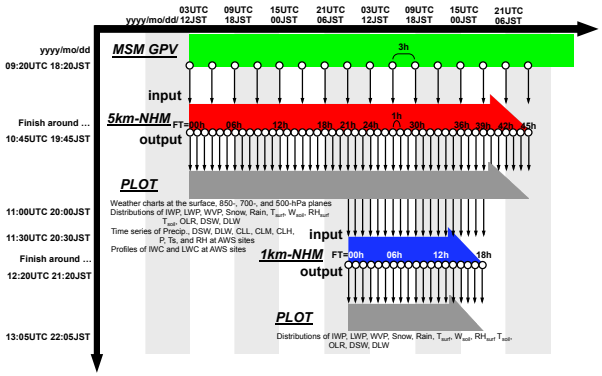

Fig. 2. Schedule for the weather prediction with the initial time of 1200 JST. Thin black arrows indicate the data flow.

The vertical grid arrangement in the 1km-NHM-D2 is the same as in the 5km-NHM, while the domain size is 700 km × 610 km. The integration time is 18 h with a timestep of 8 s. Computations of the radiative process are performed every 15 min at a horizontal grid spacing of 2 km. The initial and boundary conditions are obtained from the 5km-NHM. The same

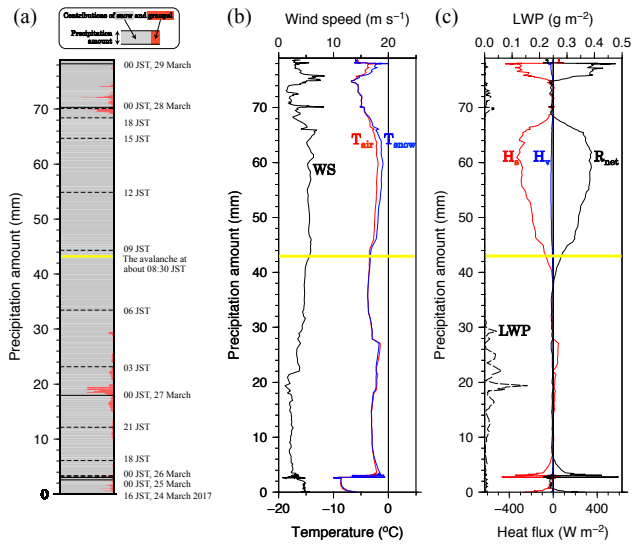

Fig. 3 Simulation results for the meteorological parameters at the avalanche site. (a) Stratigraph of water equivalent precipitation amount accumulated every 10 min from 1600 JST, 24 March 2017. Grey and red coloring indicates the respective contributions of snow and graupel particles to each 10-min precipitation amount. (b) Wind speed (black line, WS), air temperature (red line, T_{air}) and snow temperature (blue line, T_{snow}) as functions of the accumulated precipitation amount. (c) Same as (b) but for the net radiation flux (black solid line, R_{net}), sensible heat flux (red line, H_s), latent heat flux (blue line, H_v) and liquid water path (black broken line, LWP). The yellow line shows the presumed time at which the avalanche occurred.

configuration is adopted for the 1km-NHM-D3, except for the domain size, which is 650 km × 650 km. The initial time of the 1km-NHM-D2 and -D3 is 21 h later than that of the 5km-NHM (Fig. 2). The prediction results for several domestic observation sites are provided to the meteorological and glaciological research communities via a web service.

3. Computational cost

Computations are performed on the FUJITSU Supercomputer PRIMEHPC FX100 at the Meteorological Research Institute (MRI) of the JMA. Each job runs with 256 Multi Processor Interface (MPI, 32 MPI/node x 8 nodes) for the 5km-NHM simulation twice per day, which finishes in about 70 min. This costs 6,813 node-hours/year (8 nodes x 70/60 h x 2 runs x 365 days). Maximum memory usage is about 23 GB/node. For the 1km-NHM-D2 simulations, each job runs with 256 MPI (16 MPI/node x 16 nodes) twice per day, which finishes in about one and a half hours. This costs 17,520 node-hours/year (16 nodes x 1.5 h x 2 runs x 365 days). Maximum memory usage is about 22 GB/node. The computational cost for the 1km-NHM-D3 is almost same as that for the 1km-NHM-D2.

Each run of the 5km-NHM needs 29.3 GB of free disk space for I/O operation. We are archiving two-dimensional data, vertical profiles above observation sites, and plotted graphs for each simulation. The archived data size is 1.9 GB/run. This requires the storage space of 1.4 TB/year. For 1km-NHM-D2, 38.0 GB/run and 3.1 TB/year are required for running a job and archiving the data, respectively. Almost same size of disk space is required for the 1km-NHM-D3.

4. Preliminary results of the meteorological conditions for the avalanche that occurred near the Nasu Onsen Family Ski Area on 27 March 2017

On the morning of 27 March 2017, a surface avalanche hit the alpine region just behind the Nasu Onsen Family Ski Area, killing seven high school students and a teacher who were taking part in mountain skills training. In addition to the 8 killed, 40 further people were injured. Heavy snowfall had occurred at the avalanche site since the evening of the previous day. The National Research Institute for Earth Science and Disaster Resilience (NIED) reported that there was a granular snow layer at 35 cm and a layer composed of lightly compacted snow or new snow from 17 to 30 cm under the snow surface, based on the urgent in-situ snow pit survey conducted the following day (http://www.bosai.go.jp/saigai/2016/pdf/20170331_01.pdf). A weak layer was found in the lightly compacted snow layer from 22 to 25 cm under the surface. This layer was composed of weakly rimed planar crystals, in contrast to the upper and lower layers which were composed of more strongly rimed crystals. It was presumed that the layer with weakly rimed planar crystals and the subsequent short period of heavy snowfall formed an unstable snowpack.

Figure 3a shows the stratigraph of water equivalent precipitation amount at the grid point closest to “Tengu-no-hana”, the top of the avalanche slope, in the 1km-NHM-D3 simulations. The simulated snowfall was weak on 25 March and the daytime of 26 March (Fig. 3a and 3c), and the snow temperature increased during the same period (Fig. 3b), which is consistent with formation of the granular snow layer reported by the NIED. The heavy snowfall after the evening of 26 March was qualitatively well simulated. Although the simulated bulk properties of the snowfall agree well with the snow pit survey report, the simulation result did not show a change in snowfall characteristics corresponding to the transition in crystal features across the weak layer in the snowpack.

5. Summary

A numerical prediction system was established, based on the JMA-NHM for collaboration with research activities in glaciology and snow disaster prevention. The procedure of the numerical prediction is described, including the computational resources needed for performing the simulation and for archiving the data. We present preliminary results of the meteorological conditions for the avalanche near the Nasu Onsen Family Ski Area on 27 March 2017. For a comprehensive understanding of the microphysical link between snowfall and snowpack for the avalanche event, it is necessary to take a sophisticated approach to the microphysical component of the weather prediction model and to promote integrative approaches including a snowpack model.

Acknowledgement

This work was partly supported by the Joint Research Program of the Institute of Low Temperature Science, Hokkaido University, and JSPS KAKENHI Grant Number JP15H01733, JP16K01340 and JP17K18453.

References

Saito, K., T. Fujita, Y. Yamada, J. Ishida, Y. Kumagai, K. Aranami, S. Ohmori, R. Nagasawa, S. Kumagai, C. Muroi, T. Kato, H. Eito, and Y. Yamazaki, 2006: The operational JMA nonhydrostatic mesoscale model. *Mon. Wea. Rev.*, **134**, 1266–1298.

NOAA'a National Air Quality Forecast Capability for ozone and fine particulate matter

J. McQueen[1], J. Huang[1,2], H. Huang[1,2], P. Lee[3], I. Stajner[4]

1: NWS/NCEP, 2: IMSG corp., 3: NOAA/Air Resources Laboratory, 4: NWS/STI

The NOAA National Air Quality Forecast Capability, NAQFC, provides 2 day model forecasts of ozone and fine particulate matter surface concentrations twice per day at 06 and 12 UTC cycles. The NAQFC operational forecast for ozone (O_3) for the nation was implemented in September 2007 and for fine particulate matter (PM2.5) in January 2015. The NAQFC is made up of the North American Non-Hydrostatic Multiscale Model (NAM-NMMB) 12 km numerical weather prediction model and the EPA Community Model for Air Quality (CMAQ) using Carbon Bond-V (CB-V) gas phase chemistry and AERO-IV particulate processing. Predictions are available in real-time for the continental U.S., Alaska and Hawaii.

Offline coupling between NAM and CMAQ is achieved at hourly intervals by interpolation from the NAM to CMAQ horizontal and vertical grids. Anthropogenic emissions are updated monthly from the EPA National Emission Inventory for base year 2011. Wildfire smoke emissions were included in 2015 and based upon the U.S. Forest Service BlueSky smoke emission system and the NESDIS Hazardous Mapping System (HMS) fire locations updated daily. Dust emissions were also included in 2015 using a friction velocity and soil moisture criteria based approach. Dust lateral boundary conditions are provided by the NCEP NEMS Global Aerosol Capability (NGAC) V2 with climatological values from NASA GEOS-Chem for other species. The number of vertical levels was increased to 35 and an analog bias correction for PM2.5 was implemented in 2016. Predictions are available to U.S. State air quality forecasters and the public from the NWS National Digital Guidance Database (NDGD): http://airquality.weather.gov/ with experimental model predictions at: http://www.emc.ncep.noaa.gov/mmb/aq/.

NWS HYSPLIT atmospheric transport and dispersion modeling

J.McQueen[1], B. Stunder[2], A. Stein[2], H. Huang[1,3] and I. Stajner[4]

1: NWS/NCEP, 2: NOAA/Air Resources Laboratory, 3: IMSG corp., 4: NWS/STI

Understanding and predicting atmospheric transport and dispersion is essential for protecting the health and welfare of the public and emergency response personnel when harmful substances are released into the air in significant quantities. The Federal National Response Framework, approved by the President in January, 2008, assigns NOAA atmospheric transport and dispersion (ATD) prediction responsibilities for smoke and radioactive and hazardous materials, maintenance and development of Hybrid Split Puff Langrangian Integrated Trajectory Model (HYSPLIT), and coordination with the World Meteorological Organization on international incidents. The Air Resources Laboratory (ARL) develops many of NOAA's capabilities for these services.

The need for ATD or "plume" understanding and tools is continually evolving, driven by demands for more accurate predictions, estimates of uncertainties, finer spatial resolution, easier-to-use tools, and tools to address evolving risks. For instance, in 2008 the U.S. Government Accounting Office (GAO)[1] recommended that the Secretary of Homeland Security "work with the federal plume modeling community to accelerate research and development to address plume model deficiencies in urban areas and improve federal modeling and assessment capabilities. Such efforts should include improvements to meteorological information, plume models, and data sets to evaluate plume models." NCEP works with ARL's research and development (R&D) to addresses each of these areas with the HYSPLIT dispersion modeling system.

Currently, the HYSPLIT system is used to provide the following Operational atmospheric dispersion products:

- 48-hour wild-fire smoke forecasts from the daily 06 UTC cycle for CONUS, Alaska, Hawaii driven by the 12 km North American Model (NAM).
- 48-hour dust forecasts from 06 and 12 UTC cycles for CONUS
- 48-hour volcanic ash forecasts whenever requested by the International Civil Aviation Organization (ICAO)-designated U.S Volcanic Ash Advisory Centers (Washington, DC and Anchorage, Alaska). This is typically driven by NOAA Global Forecast System (GFS), although other model output can be used.
- 72-hour radiological emergency response plume forecast when requested per the World Meteorological Organization (WMO)-designated Regional Specialize Meteorological Center (RSMC) arrangements (IAEA or other country's National Meteorological Services; NMS). This is typically driven by GFS, although other model output can be used.
- 16-hour dispersion forecast for HAZMAT-type (chemical spill, explosion, etc.) incident upon the request of a WFO, almost always driven by 12-km North American Model (NAM), though other model output can be used.
- 16-hour dispersion forecasts for HAZMAT-type incidents, driven by NAM 12 km, for about 25 locations are run four times a day to support U.S. National Weather Service (NWS) Weather Forecast Office (WFO ; "canned" runs).
- 48-hour back-tracking product when requested per the WMO/RSMC arrangements. This is typically driven by GFS, although NAM can be used.

[1]GAO, 2008. First Responders' Ability to Detect and Model Hazardous Releases in Urban Areas is Significantly Limited. GAO-08-180 Homeland Security.

- HYSPLIT-formatted meteorology files are created for input to the above dispersion applications.
    - GFS (1 degree, pressure-level), GDAS(Global Data Assimilation System; 1 degree, pressure-level), NAM (hybrid-level: CONUS, Alaska, Hawaii nest, fire weather nest CONUS nest; and pressure-level: CONUS), and RAP (Rapid Refresh model; 20 km, pressure-level)
- HYSPLIT-formatted meteorology files are disseminated to ftpprd.ncep.noaa.gov, where they are
    - Automatically retrieved by the NWS Weather Operations Center (WOC) to operationally support the web-based HYSPLIT interface for NWS WFO (https://www.hysplit.noaa.gov)
    - Automatically retrieved by NOAA/ARL to support
        - a test of HYSPLIT trajectories-by-email for the NWS Fire Weather program, and
        - customers on the ARL Real-time Emergency Access and Display sYstem (READY) website (http://ready.arl.noaa.gov/).

For all applications, dispersion is simulated using either the multi- or single-processor version of the same code. The smoke and dust forecast guidance is sent in gridded form to the NOAA/MDL National Display and Graphics System (NDGD) for distribution to forecasters and emergency managers at the individual state level.

The RSMC predictions are initiated by the NCEP/SDM (Senior Duty Meteorologist) and distributed to National Forecast Centers via fax. Digital and graphical products are also shared between other country RSMCs through a protected ARL (non-operational) web page. Monthly exercises are performed by the SDM with other RSMCs.

The volcanic ash predictions are initiated by the NCEP, NESDIS/SAB (Synoptic Analysis Branch), or NWS AAWU (Alaska Aviation Weather Unit) and distributed via WAFS and made available over the Internet operationally at the AWC and non-operationally at ARL and SAB.

The HAZMAT-type output is made available on a secure NCEP server (https://hysplit.ncep.noaa.gov/). The NCEP AWC is able to initiate a HAZMAT-type.

Recently, HYSPLIT was improved to meet the NCEP requirements for volcanic ash product dissemination, and meet NOAA requirements for back-tracking support to the Comprehensive Test Ban Treaty Organization (CTBTO). Improvements were accomplished mainly by upgrading the wet deposition scheme for radiological materials and volcanic ash.

Consistent Initial and Lateral Boundary Perturbations in Mesoscale Ensemble Prediction System at JMA

Kosuke Ono
Numerical Prediction Division, Japan Meteorological Agency, Tokyo, Japan
E-mail: kou.ono@met.kishou.go.jp

1. Motivation

The Japan Meteorological Agency (JMA) started pre-operation of the regional ensemble prediction system (Mesoscale Ensemble Prediction System: MEPS) in March 2015 with the aim of providing uncertainty information for operational deterministic regional model (Meso-Scale Model: MSM). MEPS is based on the JMA non-hydrostatic model (JMA-NHM; Saito. et al. 2006) with 5 km grid spacing, 48 vertical layers and the ensemble size of 11 including a control run (CTL)[1].

The initial perturbations (IPs) of MEPS members are generated by blending singular vectors (SVs) at different scales; global SV (GSV) based on JMA global model (Global Spectral Model: GSM), and mesoscale SV (MSV) based on JMA-NHM (Ono et al. 2011[2]). However, the lateral boundary perturbations (LBPs) are derived from JMA global ensemble prediction system (Global EPS: GEPS). This combination of individually generated IPs and LBPs brings inconsistencies between them, including artificial anomalies from the CTL forecast in perturbed runs. Figure 1 shows an example of such inconsistencies. One of perturbed runs (member 09: M09) forecasts heavy precipitation over China (see dashed black circle in Figure 1) at T+12. This precipitation is heavier than that from CTL, corresponding to the positive perturbation of equivalent potential temperature (EPT) at 925 hPa originating from IP. At T+18, heavy rain is still forecast with CTL near the same region. However, the precipitation forecast with M09 is weaker because the negative perturbation of EPT at 925 hPa from the western lateral boundary is dominant in this region. As this example shows, inconsistencies between IP and LBP can change the tendency of perturbed forecasts artificially. It can be an obstacle to the use of ensemble members as different scenarios from CTL.

To maintain consistency between IP and LBP, a new LBP generation method has been developed. This approach is based on the integration of GSV (a large-scale component of IP), using the tangent linear model (TLM).

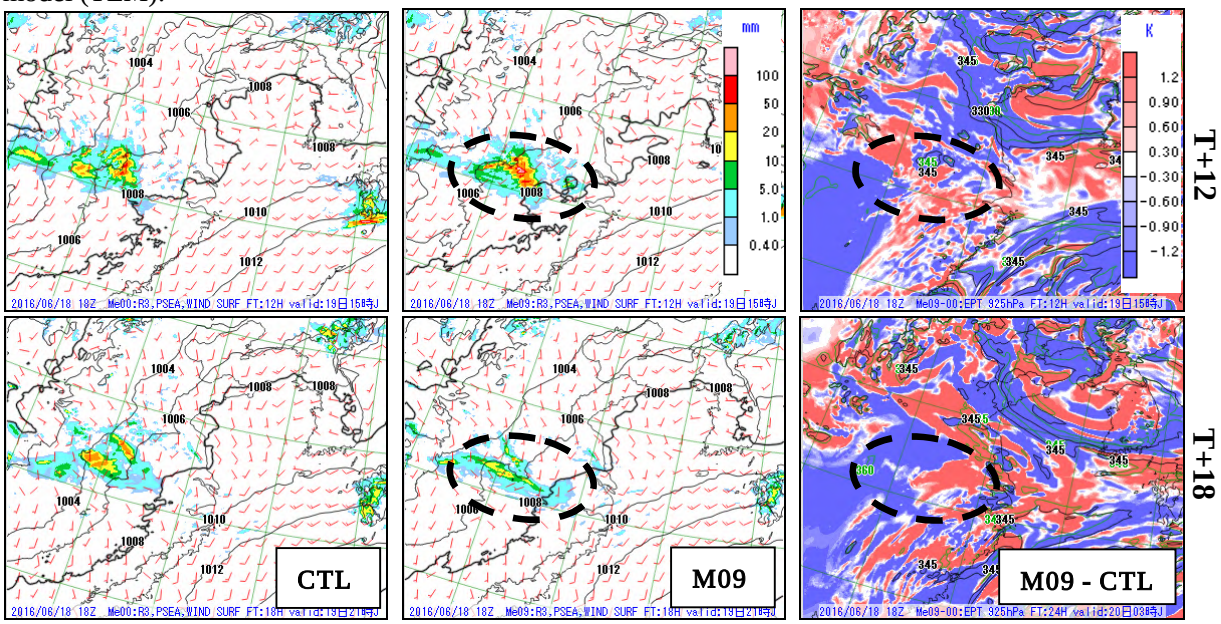

Figure1: Sea level pressure, surface wind and three hour accumulated rainfall foreacast with CTL (left) and M09 (center). M09 perturbation of EPT at 925 hPa is also shown (right). The initial time is 18 UTC on 18 June 2016.

2. New Configurations of GSV in Consideration of LBP

The use of GSV for both IP and LBP requires coverage of the whole forecast domain over the 39-hour forecast period by GSV. Accordingly, the GSV target region was extended to exceed the forecast domain

[1] A new non-hydrostatic model ASUCA (Aranami et al. 2015) with 76 vertical layers has replaced JMA-NHM as the MSM forecasting model since Feb. 2017. Therefore, JMA plans to also switch the forecasting model of MEPS to ASUCA soon.

[2] Water vapor perturbation from GSV is not used in the current system.

(Figure 2 (a)). Its optimization interval was also extended from 24 to 39 hours in line with the forecast range. For LBP generation, all GSVs are integrated over a period of 39 hours using the TLM, and combined linearly with the coefficients used in IP generation for each forecast time. The LBP amplitude is adjusted using the climatological root mean square error (RMSE) of the lateral boundary value (same as GSM forecast) against the MSM initial value. Figure 2 (b) illustrates the relationship between SVs and perturbations.

Figure 3 highlights the consistency between IP and LBP structures at T+3. The LBP from GEPS induces discontinuity in the perturbation pattern shaped like a 'frame' near the lateral boundary. Meanwhile, the GSV-based LBP exhibits clear continuity with IP. To determine the impact of enhanced consistency, deterministic forecast skill scores were calculated for all ensemble members, and compared with those of CTL and each member using LBP from GEPS. However, no clear advantage from the new system was found, suggesting that consistency does not improve the statistical forecast skill score of each member.

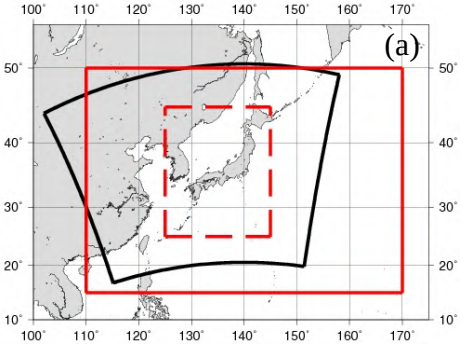

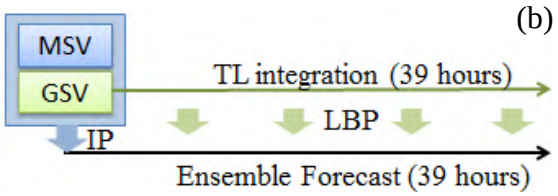

Figure 2: (a) Forecast domain (black line), and target region (red lines; dashed: old region; solid: new region). (b) Relationship between SVs and perturbations.

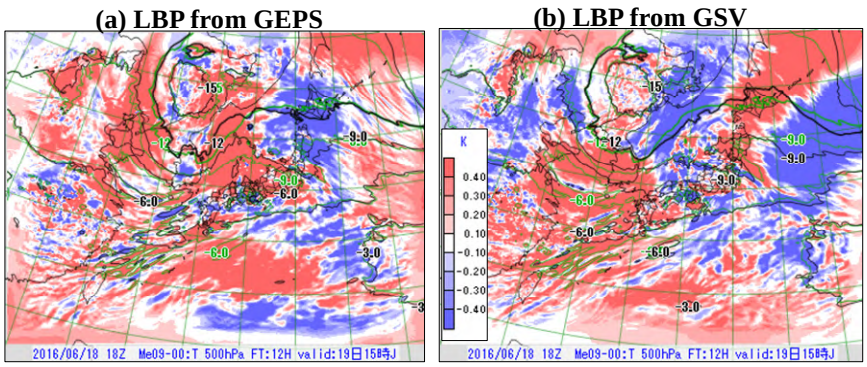

Figure 3: 500-hPa temperature perturbation at T+3 (initial time: 18 UTC on 18June 2016 (a) LBP from GEPS. (b) LBP from GSV.

3. Probabilistic Forecast Skill Scores for the New GSV System

The changes in GSV influence IP, and the performance of MEPS as an ensemble prediction system. The spread-skill relationship and Brier skill score (BSS) for precipitation forecasting are shown in Figure 4. The excessive spread of LBP with the old GEPS system is suppressed in LBP with the new GSV system. BSS is also improved by suppressing excessive dispersion in rain forecasts. This LBP method was incorporated into the pre-operational system in January 2017.

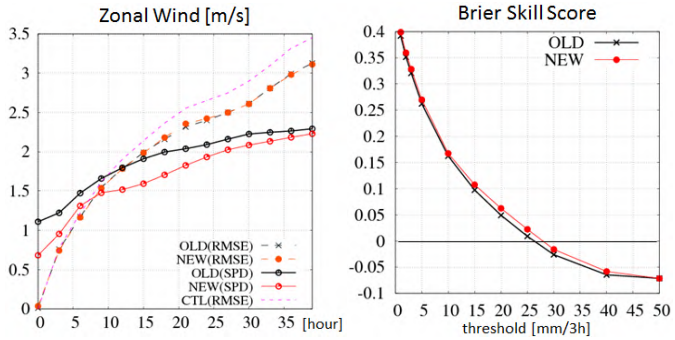

Figure 4: Ensemble spread (SPD) and RMSE against MSM initial value of zonal wind at 500 hPa (left) and BSS of three-hour accumulated rainfall against rain gauge data (right). The black line shows the LBP with the old GEPS system, and the red line shows that with the new GSV system. The pink line shows the RMSE of CTL. The verification period is 17 - 26 June 2016 with every 18 UTC initial forecast (10 cases).

References

Aranami et al. (2015): A new operational regional model for convection-permitting numerical weather prediction at JMA. *CAS/JSC WGNE Res. Activ. Atms. Oceanic. Modell.*, **45**, 5.05-5.06.

Ono el al. (2011): A mesoscale ensemble prediction system using singular vector methods. *CAS/JSC WGNE Res. Activ. Atmos. Oceanic. Modell.*, **41**, 5.17-5.18.

Saito et al. (2006): The operational JMA Nonhydrostatic Mesoscale Model. *Mon. Wea. Rev.* **134**, 1266-1298.

Upgrades to the NCEP North American Mesoscale (NAM) System

E. Rogers[1], J. Carley[2], B. Ferrier[2], E. Aligo[2], G. Gayno[2], Z. Janjic[1], Y. Lin[1], S. Liu[2], G.P. Lou[2], M. Pyle[1], W-S. Wu[1], Y. Wu[2], and **G. DiMego[1]**

[1]NCEP/EMC, College Park, MD
[2]IMSG – NCEP/EMC, College Park, MD

A major upgrade to the NCEP North American Mesoscale Forecast System (NAM) was implemented on 21 March 2017. This upgrade targeted the greatest deficiencies in the previous NAM system, such as excessive precipitation from the high-resolution CONUS nest and risks of failure exposed by Hurricane Joaquin. The development and testing of the NAM upgrade targeted these deficiencies with following changes:

1) **Resolution changes:** CONUS Nest from 4 km to 3 km, Alaska nest from 6 km to 3 km, CONUS Fire-weather nest from 1.333 km to 1.5 km
2) **Forecast model changes:**
   - Updated microphysics : improved stratiform precipitation, better anvil reflectivity, lower peak reflectivity, reduce areas of light/noisy reflectivity, significantly reduce CONUS nest high precipitation bias in the warm season
   - "Stability" changes : more frequent calls to physics, update specific humidity every model time step, calculate cloud condensation every time step, mix out superadiabatic layers
   - Changes in parameterized convection for the 12 km parent domain to improve low QPF bias in cool season
   - Radiation and land-surface physics changes to reduce 2-m temperature warm bias in summer, reduce high 2-m dew point temperature bias in cool season, and visibility forecast in coastal regions
3) **Data Assimilation (DA) changes :**
   - Replace 12-h DA with 3-h analysis/forecast updates for the 12 km parent domain with a 6-h DA cycle with hourly analysis forecast updates for the 12 km parent, 3 km CONUS nest, and 3 km Alaska nest domains
   - Use of lightning and radar reflectivity-derived temperature tendencies in the diabatic digital filter initialization
   - Assimilate new satellite radiance and cloud drift wind data
4) **Other science changes**
   - Tropical cyclone relocation in the 12 km domain
   - Reinstate use if USAF 557th Weather Wing (formerly AFWA) snow depth analysis
   - Use of a fresh water lake temperature climatology for the CONUS, Alaska, and Fire Weather nests
   - Use NESDIS burned area data in the fire weather nest to adjust greenness fraction, albedo, and top layer soil moisture

The NAM changes led to greatly improved warm-season precipitation forecasts from the 3 km model simulations (Figure 1), improved predictions of low visibility conditions in coastal regions, improved cool-season precipitation forecasts from the 12 km simulation, improved short-term (0-12 h) simulation of convective storms in the 3 km simulation (Figure 2), and a reduction of the moist bias for CONUS cool-season surface dew point temperatures and a reduction of the warm bias for CONUS summer surface temperatures.

This is the last science upgrade to the NAM forecast system as the EMC mesoscale modeling/data assimilation team will focus their efforts on developing high-resolution forecast systems based on the FV3 dynamic core.

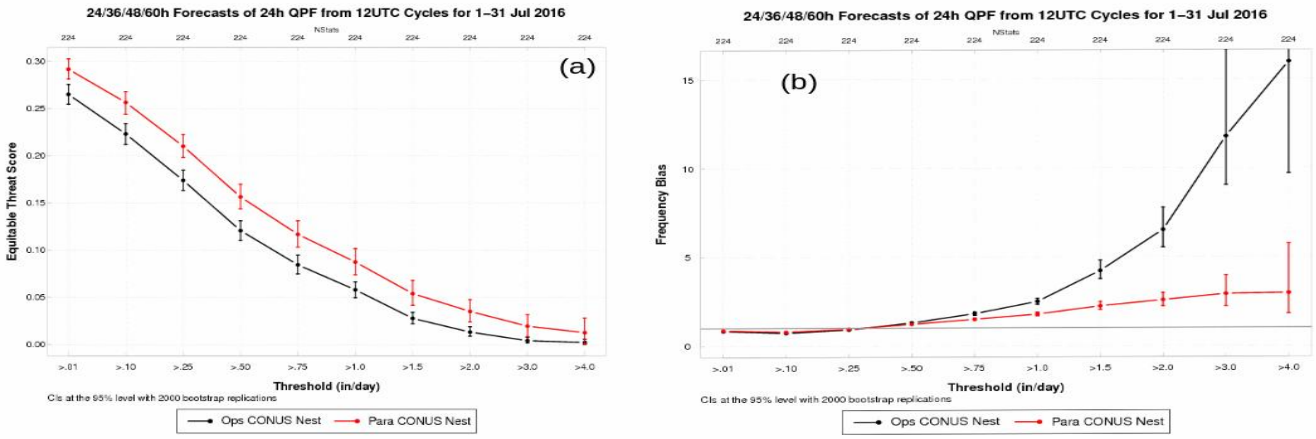

Figure 1: (a) CONUS 24-h forecast precipitation equitable threat score for all 1200 UTC runs of the operational 4 km CONUS nest (black) and the parallel 3 km NAMv4 CONUS nest (red) from 1-31 July 2016. (b) Same as (a) but for bias.

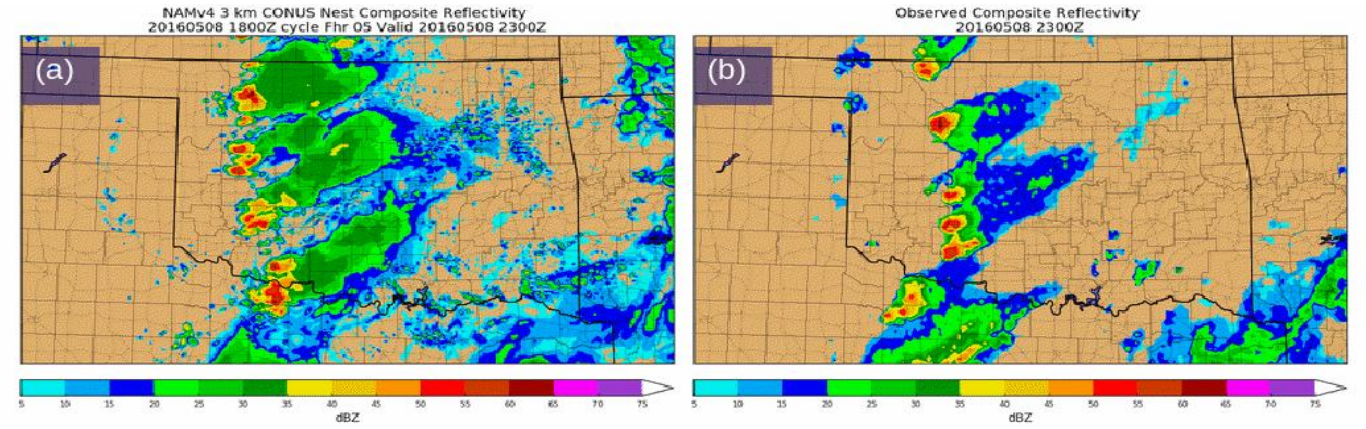

Figure 2: (a) 5-h forecast of composite reflectivity (dBZ) from the 1800 UTC 8 May 2016 run of the NAMv4 3 km CONUS nest valid at 2300 UTC 8 May 2016. (b) Observed composite reflectivity (dBZ) valid at 2300 UTC 8 May 2016.

Numerical simulations of convective bursts occurred just before landfall of Typhoon Lionrock (2016)

*Akiyoshi Wada and Ryo Oyama
[1]Meteorological Research Institute, Tsukuba, Ibaraki, 305-0052, JAPAN
*awada@mri-jma.go.jp

1. Introduction

Typhoon Lionrock was the ninth tropical cyclone in the typhoon season of 2016. According to the Regional Specialized Meteorological Center (RSMC) Tokyo best track analysis, the typhoon was generated around 29.2˚N, 133.3˚E at 1200 UTC on 21 August 2016 and reached the minimum central pressure of 940 hPa around 27.7 ˚N, 137.9˚E at 0600 UTC on 28 August. Then, the typhoon made landfall in the northern region of Japan just before 1200 UTC on 30 August (http://web.archive.org/web/20160830092234/http://www.jma.go.jp/jp/typh/D20160830090017754.html).

During the mature phase of Lionrock that was moving northwestward, Himawari-8 infrared channel (10.4 μm) temperature brightness images captured convective bursts ahead of the typhoon that occurred on the downstream side. In order to clarify the formation process of the precipitation pattern, numerical simulations were performed by using a nonhydrostatic atmosphere model coupled with ocean and ocean wave models (CPL: Wada, 2010).

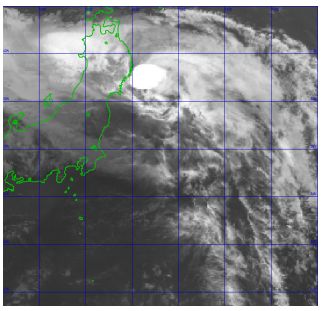

Figure 1 Himawari-8 infrared channel (10.4 μm) temperature brightness image at 0730 UTC on 30 August.

2. Data and method

Figure 2 shows the computational domain. It covered a 3000 km x 3000 km area with a horizontal grid spacing of 3 km. The integration time was 210 hours with the time steps of 3 seconds in the nonhydrostatic atmosphere model, 18 seconds in the ocean model and 10 minutes in the ocean wave model in the CPL. The initial time was 0000 UTC on 23 August in 2016. The nonhydrostatic atmosphere model had 55 vertical levels with variable intervals from 40 m from the near-surface layer to 1013 m for the uppermost layer. The top height was ~26 km. The simulations used the Japan Meteorological Agency global objective analysis data for atmospheric initial and boundary conditions (with a horizontal grid spacing of ~20km) and the daily oceanic reanalysis data calculated by the Meteorological Research Institute multivariate ocean variational estimation (MOVE) system (Usui, et al. 2006) with a horizontal grid spacing of 0.5˚. The interval of model output was 1 hour from the initial time to 108 hours and was 20 minutes after 108 hours.

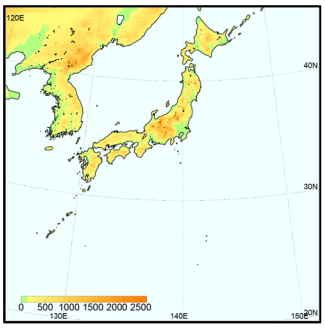

Figure 2 Computational domain. Colors indicate land elevation.

3. Results

3.1 Track and central-pressure simulation

Figure 3a shows the results of track simulations for Lionrock with central pressures simulated by the CPL together with RSMC best track data. According to RSMC best track data, the Lionrock moved southwestward and then changed the direction to eastward and then moved northeastward. The typhoon again changed the direction to north northwestward and then made landfall in the northen region of Japan. The track was successfully simulated by the CPL. Figure 3b showed the time series of best track central pressures and central pressures simulated by the CPL. The best track data indicated that Lionrock underwent rapid intensification from the initial time to 1800 UTC on 24 August and then kept the central pressure of 945 hPa. However, the simulated typhoon continued to rapidly intensity till 1800 UTC on 25 August although the maximum wind speeds kept the value from 0000 UTC to 1200 UTC on 25 August (Figure 3c).

This study addresses the change in simulated central pressure and maximum surface winds during the mature phase. At 0600 UTC on 30 August, maximum surface winds increased and the increasing rate of simulated central pressure decreased. The time corresponded to the time when convective bursts were observed (Figure 1)

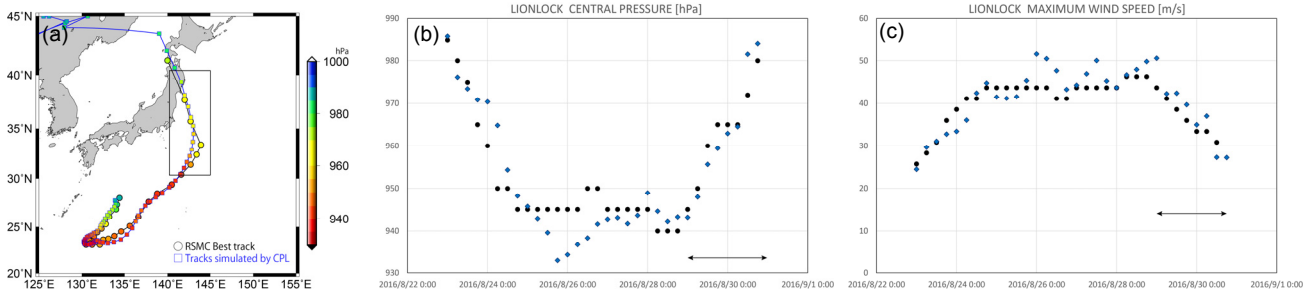

Figure 3 (a) Results of track simulations of Lionrock with simulated central pressures simulated by CPL together with RSMC best track data every three hours. (b) Time series of best track central pressures and central pressures simulated by CPL every six hours. (c) Same as (b) except for maximum wind speeds. Arrows in (b) and (c) indicated the period of mature phase that is focused on in this study.

3.2 Convective bursts and role of the ocean

Figure 4 shows more detailed time series of RSMC best track and simulated central pressure (Figure 4a) and maximum surface winds (Figure 4b) from 0000UTC on 29 August. The increasing rate of simulated central pressure decreased around 0600 UTC on 20 August, while keeping the maximum surface winds. Figure 5 shows the horizontal distributions of sea surface temperature (SST) with surface winds vectors and sea-level pressures at the interval of 4 hPa simulated by the CPL at 0000 UTC (Figure 5a) and 0600 UTC (Figure 5b) on 30 August. On the right hand side of the track of Lionrock, SST increased and the value was over 27 ˚C behind the typhoon due to near-inertial currents induced by the typhoon. The result suggests that the increase in SST was related to the decrease in the increasing rate of simulated central pressure.

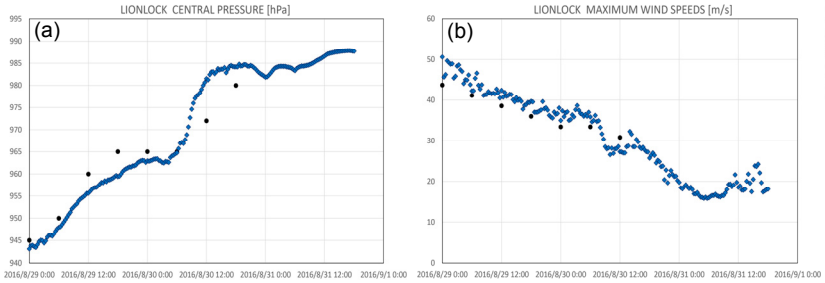

Figure 4 Same as Figure 3 except for the period from 0000UTC on 29 August at the interval of 20 minutes.

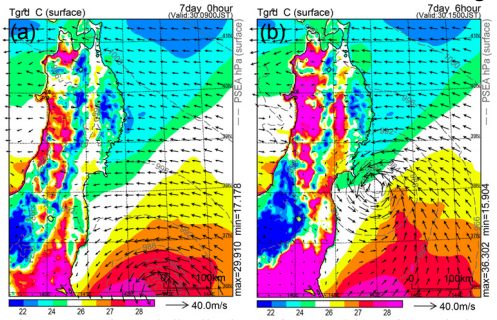

Figure 5 Horizontal distributions of SST with surface winds vectors and sea level pressures at the interval of 4 hPa simulated by the CPL at (a) 0000 UTC and (b) 0600 UTC on 30 August.

Figure 6 shows the horizontal resolution of total water content from the surface to ~17.5 km and the horizontal distributions of vertical velocity and potential vorticity at 8 km. Total water content was locally high at the quadrant of the moving direction of the storm. The high water-content area corresponded to the area where upward motion was locally dominant. This suggests that abundant water content was transported from the lower troposphere through locally strong upward motion. However, potential vorticity was relatively high in the inner core of the storm. In addition, potential vorticity was negative at the high water content area with locally strong upward vertical velocity. Thus convective bursts and associated cloud physics and dynamics contributed to the suppression of the dissipation. Thus, the storm could make landfall while keeping the intensity.

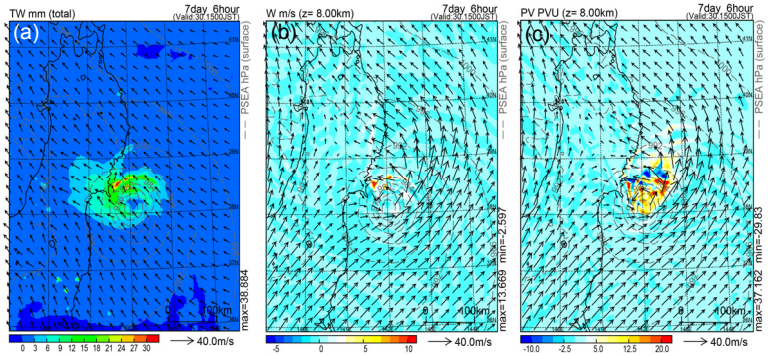

Figure 6 Same as Figure 5 except for (a) total water content from the surface to ~17.5 km with winds vectors at ~17.5 km, (b) vertical velocity with wind vectors at 8 km and (c) potential vorticity at 8 km with wind vectors at 8 km at 0600 UTC on 30 August.

4. Concluding remarks

This study addresses convective bursts occurred just before making landfall of Lionrock in the northern region of Japan. The numerical simulation performed by the CPL reasonably reproduced convective bursts at the quadrant of the moving direction of the typhoon. This feature was consistent with the observations. Warm water advected due to near-inertial currents enhanced by the storm was simulated at the timing of the decrease in the increasing rate of simulated central pressure. Convective bursts had locally high water content and negative potential vorticity, while potential vorticity was positive in the inner core of the storm.

These features were poorly simulated by a nonhydrostatic model with fixed SST given as a boundary condition although the simulated central pressure was extremely low (not shown). This implies that the oceanic response to Lionrock was related to the formation of convective bursts. Previous study using the same CPL reported that a similar rapid intensification occurred in the case of Typhoon Man-yi in 2013. Wada (2015) could not reproduce convective bursts realistically when the coupled model was used. The relation of convective bursts to rapid intensification and the dependence of the relation on geographical location will be a subject in the future as well as clarification of more detailed processes of convective bursts and their relation to typhoon-ocean interactions.

Acknowledgements

This work was supported by JSPS KAKENHI Grant Number JP15K05292.

References

Makihara Y (1996). A method for improving radar estimates of precipitation by comparing data from radars and raingauges. J Meteor Soc Japan 74:459-480.

Usui, N., S. Ishizaki, Y. Fujii, H. Tsujino, T. Yasuda and M. Kamachi (2006). Meteorological Research Institute multivariate ocean variational estimation (MOVE) system: Some early results. Advances in Space Research, 37(4), 806-822.

Wada A. (2015). Unusually rapid intensification of Typhoon Man-yi in 2013 under preexisting warm-water conditions near the Kuroshio front south of Japan. Journal of Oceanography, 71, 597–622.

Wada, A., N. Kohno and Y. Kawai (2010). Impact of wave-ocean interaction on Typhoon Hai-Tang in 2005. SOLA, 6A, 13-16.

Sensitivity numerical simulations of Hurricane Patricia (2015) on lateral boundary conditions and inhibition rate of evaporation

Akiyoshi Wada
Meteorological Research Institute, Tsukuba, Ibaraki, 305-0052, JAPAN
awada@mri-jma.go.jp

1. Introduction

Hurricane Patricia (2015) was a historic tropical cyclone (TC) that broke historical records such as intensification rate during the intensification phase, maximum intensity during the mature phase and weakening rate during the decaying phase in late October 2015 in the eastern North Pacific (Rogers et al., 2017). Rogers et al (2017) pointed out that the storm was extremely small so that it could not be well-depicted using a numerical model grid with a grid spacing of 2-3 km. In addition, the simulation of the storm could be affected by experimental design such as the width of a sponge layer for lateral boundary condition, which is necessary for a regional atmosphere model, and values of parameters associated with cloud physics. Thus, we performed sensitivity numerical simulations of Patricia to the width of the sponge layer for lateral boundary condition and inhibition rate of evaporation of rain, snow and graupel by using a nonhydrostatic atmosphere model (NHM) with a grid spacing of 1 km.

2. Data and method

Figure 1 shows the computational domain. It covered a 1080 km x 1080 km area with a horizontal grid spacing of 1 km. The integration time was 48 hours and the initial time was 0600 UTC on 22 October in 2015. NHM had 55 vertical levels with variable intervals from 40 m for the near-surface layer to 1013 m for the uppermost layer. The top height was ~26 km. The simulations used the Japan Meteorological Agency global objective analysis data (with a horizontal grid spacing of ~20km) for creating atmospheric initial and boundary conditions and the daily oceanic reanalysis data calculated by the Meteorological Research Institute multivariate ocean variational estimation (MOVE) system (Usui, et al. 2006) with a horizontal grid spacing of 0.5˚.

For sensitivity numerical experiments, the width of the sponge layer (IDIFX) was set to 10, 40 and 70, respectively (see Table 1). The inhibition rate of evaporation of rain, snow and graupel was set to 0.0, 0.5 and 1.0, respectively. The control run (CNTL) was defined with IDIFX=10 and the value of the inhibition rate=0.0.

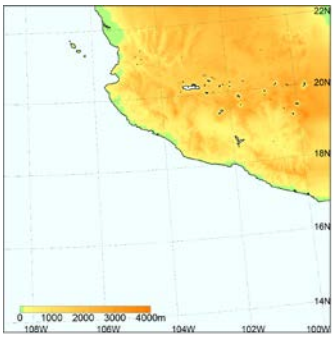

Figure 1 Computational domain. Colors indicate land elevation.

3. Results

3.1 Track and central-pressure simulation

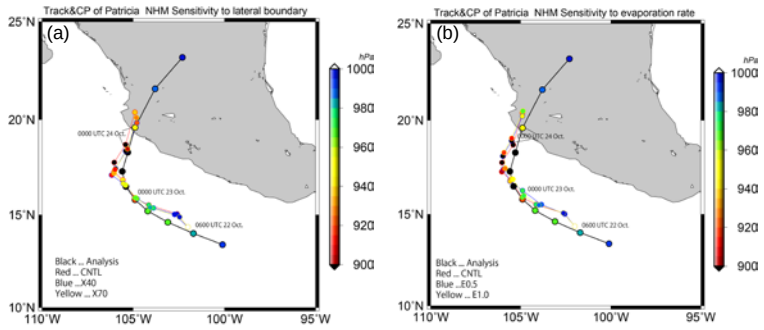

Figure 2 Results of track simulations of Patricia for (a) sensitivity to lateral boundary conditions and (b) inhibition rate of evaporation.

Figure 2 shows the results of track simulations. The width of the sponge layer (Figure 2a) and the value of inhibition rate (Figure 2b) were not sensitive to the simulated tracks. All simulated tracks had a northward bias at an earlier integration time, and then they had a westward bias after the recurvature. Less sensitivity of track simulations to these parameters indicates that these biases and slow translation were caused by atmospheric initial conditions used in the simulations.

Figure 3 shows the results of the simulations of central pressure and maximum surface wind speed. All simulations poorly depicted the early rapid intensification and peak intensity at 1200 UTC on 23 October. However, the simulations well depicted the weakening rate during the decaying phase although the timing was late due to slow translation of simulated storm.

Table 1 Control and sensitivity experiments

Experiment	IDIFX	Inhibition rate (rain, snow, graupel)
CNTL (X10,E0.0)	10	0.0
X40	40	0.0
X70	70	0.0
E0.5	10	0.5
E1.0	10	1.0

Figure 3 Results of the simulations of central pressure and maximum surface wind speed for (a) sensitivity to lateral boundary conditions and (b) inhibition rate of evaporation.

3.2 Sensitivity of the inner-core structure to lateral boundary conditions and evaporation rate

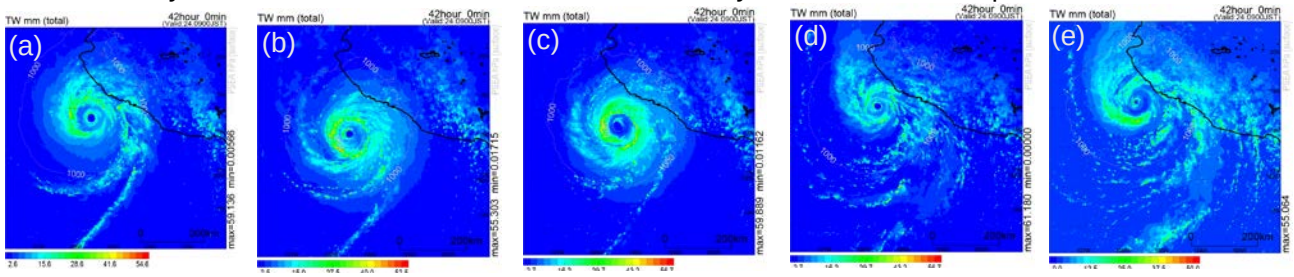

Figure 4 Horizontal distributions of total water content (shades) in a grid column from the surface to the 44th level in (a) CNTL, (b) X40, (c) X70, (d) E0.5 and (e) E1.0 experiments at 42h (corresponding to 0000 UTC 24 October). Contour intervals are 40 hPa.

Figure 4 shows the horizontal distributions of total water content in each experiment at the 42-hour integration time (42h), corresponding to 0000 UTC 24 October. The distributions quite differed among the five experiments. Some experiments depicted a distinct double eyewall structure (Figs. 4a, 4d and 4e), which is consistent with AMSR-2 89GHz brightness temperature image (Fig.11 in Rogers et al., 2017). A relatively large width of the sponge layer inhibited the formation of the inner distinct eyewall structure. A larger number of the inhabitation rate of evaporation of rain, snow and graupel did affect a smaller size of the inner distinct eyewall structure although the storm intensity in the CNTL experiment was stronger than that in the E1.0 experiment. The smaller size of the inner distinct eyewall structure is consistent with AMSR-2 89GHz brightness temperature image (Fig.11 in Rogers et al., 2017). The results suggest that experimental design of numerical simulation for TCs is important to depict the intensity and the inner core structure. It should be noted that spiral rainbands outside the inner core of the TC became remarkable in the E0.5 and E1.0 experiments, while the intensity was relatively weak.

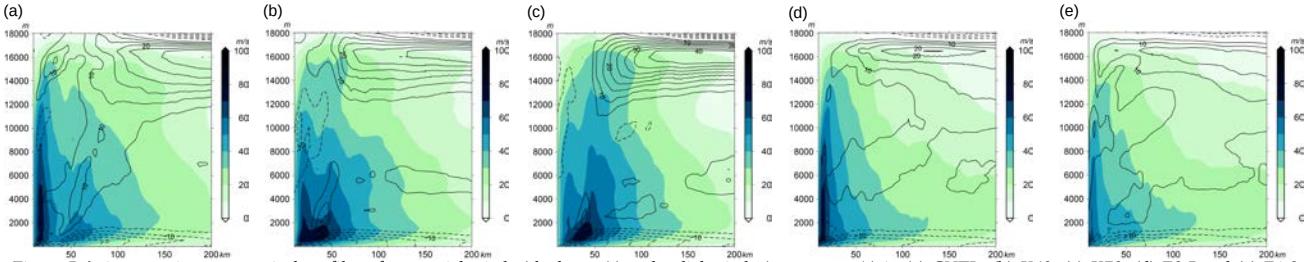

Figure 5 Axisymmetric mean vertical profiles of tangential winds (shades: m/s) and radial winds (contours: m/s) in (a) CNTL, (b) X40, (c) X70, (d) E0.5 and (e) E1.0 experiments at 42h (corresponding to 0000 UTC 24 October). Solid contours indicate outflow, while dashed contours indicate inflow (to the TC center). Contour intervals are 5 m/s.

Figure 5 shows axisymmetric mean vertical profiles of radial and tangential flows in each experiment at 42h. The CNTL experiment depicted a distinct double eyewall structure, which is consistent with the result of composite analysis in Rogers et al. (2017). The inner eyewall became weaker as the width of the sponge layer increased. The location of the outer eyewall changed inward so that the outer eyewall was dominant in the X70 experiment. This suggests that the atmospheric environment could affect the eyewall replacement process. The outer eyewall was not well simulated in the E0.5 and E1.0 experiments. In the E1.0 experiment, both primary and secondary circulations became weak. The result indicates that the inhibition of evaporation of rain, snow and graupel played a crucial role in weakening the TC.

4. Concluding remarks

Hurricane Patricia was a historic tropical cyclone in view of the intensification rate, maximum intensity and weakening rate during the decaying phase and its storm size was extremely small. NHM with a grid spacing of 1 km was used for investigating the sensitivity of numerical simulations to the width of the sponge layer and inhibition rate of evaporation of rain, snow and graupel. These two factors did affect the intensity simulations and the inner-core structure. This study did not consider the effect of ocean coupling because of slow translation of simulated storm and resultant excessive TC-induced sea surface cooling simulated by a coupled atmosphere-wave-ocean model (Wada et al., 2010). To reduce the bias of the simulation of Patricia, oceanic initial conditions should be improved in addition to understanding of the role of physical processes and atmospheric boundary conditions in TC simulations.

Acknowledgements
This work was supported by JSPS KAKENHI Grant Number JP15K05292.

References

Rogers R. F., S. Aberson, M. M. Bell, D. J. Cecil, J. D. Doyle, T. B. Kimberlain, J. Morgerman, L. K. Shay and C. Velden (2017) Re-writing the tropical record books: The extraordinary intensification of Hurricane Patricia (2015), Bulletin of the American Meteorological Society, doi: 10.1175/BAMS-D-16-0039.1.

Usui, N., S. Ishizaki, Y. Fujii, H. Tsujino, T. Yasuda and M. Kamachi (2006). Meteorological Research Institute multivariate ocean variational estimation (MOVE) system: Some early results. Advances in Space Research, 37(4), 806-822.

Wada, A., N. Kohno and Y. Kawai (2010). Impact of wave-ocean interaction on Typhoon Hai-Tang in 2005. SOLA, 6A, 13-16.

Numerical simulations of shield-like precipitation pattern in the Eastern China Sea remotely enhanced by Typhoon Nepartak (2016)

*Akiyoshi Wada[1], Hiroshige Tsuguti[1] and Hiroyuki Yamada[2]
[1]Meteorological Research Institute, Tsukuba, Ibaraki, 305-0052, JAPAN
[2]University of the Ryukyus, Nakagami-gun, Okinawa, 903-0213 JAPAN
*awada@mri-jma.go.jp

1. Introduction

Typhoon Nepartak was the first tropical cyclone in the typhoon season of 2016. According to the Regional Specialized Meteorological Center (RSMC) Tokyo best track analysis, the typhoon was generated around 8.9˚N, 144.9˚E and reached the minimum central pressure of 900 hPa at 0600 UTC on 6 July in 2016. Then, the typhoon made landfall in Taiwan at 2150 UTC on 7 July (https://en.wikipedia.org/wiki/Typhoon_Nepartak_(2016)).

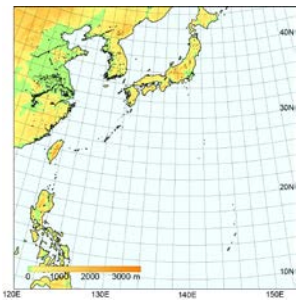

During the west northwestward translation of Nepartak, distant rainbands induced by the typhoon propagated toward the Amami Islands. The rainbands formed a shield-like precipitation pattern in the Eastern China Sea. Then the precipitation pattern formed a low pressure area that caused heavy rainfalls in the southern part of Kyusyu. In order to clarify the formation process of the precipitation pattern, numerical simulations were performed by using a nonhydrostatic atmosphere model coupled with ocean and ocean wave models (Wada, 2010). Hereafter, the atmosphere model is called NHM and the coupled model is called CPL.

2. Data and method

Figure 1 shows the computational domain. It covered a 4140 km x 4140 km area with a horizontal grid spacing of 3 km. The integration time was 120 hours with the time steps of 3 seconds in the NHM, 18seconds in the ocean model and 10 minutes in the ocean wave model. The initial time was 1800 UTC on 4 July in 2016. NHM had 55 vertical levels with variable intervals from 40 m for the near-surface layer to 1013 m for the uppermost layer. The top height was ~26 km. The simulations used the Japan Meteorological Agency global objective analysis data for atmospheric initial and boundary conditions (with a horizontal grid spacing of ~20km) and the daily oceanic reanalysis data calculated by the Meteorological Research Institute multivariate ocean variational estimation (MOVE) system (Usui et al. 2006) with a horizontal grid spacing of 0.5˚. The control and sensitivity experiments were shown in Table 1. For sensitivity numerical experiments, the Kain-Fritsch cumulus parameterization was used in the KF experiment to perform numerical simulations by the NHM and CPL. The inhibition rate of evaporation of rain, snow and graupel was set to 0.3 (EVP03), 0.5 (EVP05) and 0.7 (EVP07), respectively.

Table 1 Control and sensitivity experiments. KF indicates the Kain-Fritsch parameterization scheme.

Experiment	KF	Inhibition rate (rain, snow, graupel)
CNTL	No	0.5
KF	Yes	0.5
EVP03	No	0.3
EVP07	No	0.7

3. Results

3.1 Track and central-pressure simulation

Figure 2 shows results of track and central pressure simulations for 120 hours started from 1800 UTC on 4 July. The simulated tracks had southward biases at an earlier integration time and then changed the direction northwestward so that the simulated typhoon made landfall in the northern Taiwan region. The peak intensity represented by minimum central pressure was well reproduced in the KF experiment (873 hPa) when the NHM was used for the simulation. However, the lowest minimum central pressure was 903.6hPa in the EVP03 experiment when the CPL was used. The cumulus parameterization did affect track and central pressure simulations even when the CPL was used. For Nepartak case, errors in the KF experiment became increased compared with those in the other three experiments (CNTL, EVP03 and EVP07). It should be noted that the time of the peak intensity of the RSMC best track analysis was later than that simulated by the NHM and CPL in all four experiments. In particular, the time of the peak intensity simulated by the CPL was fastest due to the effect of sea surface cooling induced by the simulated typhoon. The error associated with the intensity change was considered to affect the simulation of the shield-like precipitation pattern.

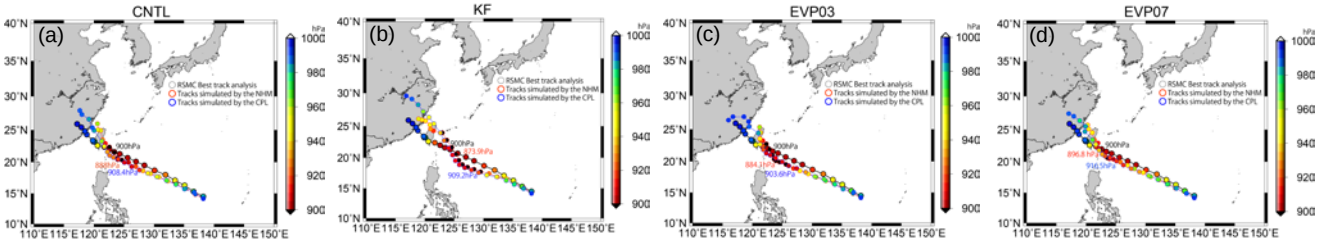

Figure 2 Results of track simulations of Nepartak with simulated central pressures in (a) CNTL, (b) KF, (c) EVP03 and (d) EVP07 simulated by the NHM and CPL, respectively. The RSMC best track was overlaid with black circles in the panels. Red circles indicated results by the NHM, while blue circles indicated those by the CPL.

3.2 Simulated shield-like precipitation pattern

Figure 3(a) shows the horizontal distributions of hourly precipitation at 1500 UTC on 7 July depicted from the Radar-Raingauge analyzed precipitation dataset estimated on the basis of radar observations calibrated with rain-gauge measurements from the Japan Meteorological Agency (JMA) Automated Meteorological Data Acquisition System (Makihara 1996). A shield-like precipitation pattern propagated northward far from the Nepartak existed around the Amami Islands. The CNTL experiment captured a shield-like precipitation pattern to some extent although the simulated pattern was located in the Eastern China Sea (Figure 3b). In the KF experiments, the precipitation pattern looked like a spiral distant rainband extending to the east and west (Figure 3c). The precipitation area was advected by southwesterly winds that were a part of the cyclonic circulation of Nepartak. The extent of the precipitation area was related to the inhibition rate of evaporation of rain, snow and graupel. In the EXP03 experiment, the area was relatively small (Figure 3d), while it was relatively large in the EXP07 experiment (Figure 3e). In Figures 3b-e, the impact of the KF parameterization on the precipitation pattern was outstanding.

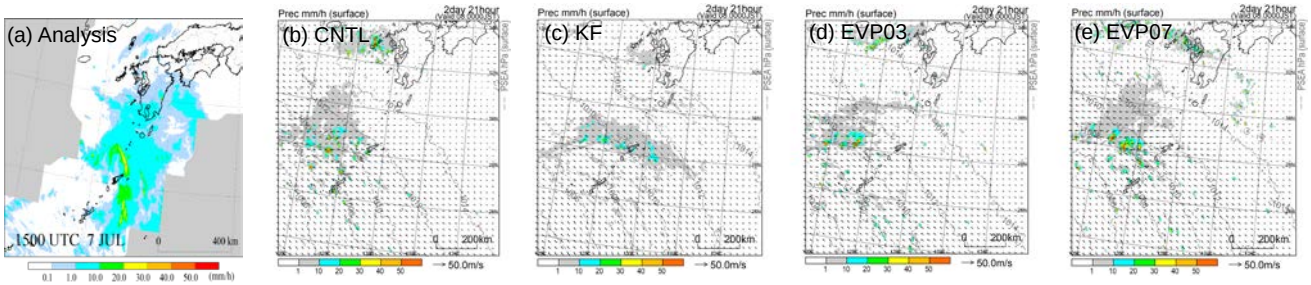

Figure 3 Horizontal distributions of hourly precipitation (shades) with sea-level pressures (contours) at 1500 UTC on 7 July in (a) the Radar-Raingauge analyzed precipitation dataset estimated on the basis of radar observations calibrated with rain-gauge measurements, (b) CNTL, (c) KF, (d) EVP03 and (e) EVP07 simulated by the CPL. Contour intervals are 2 hPa.

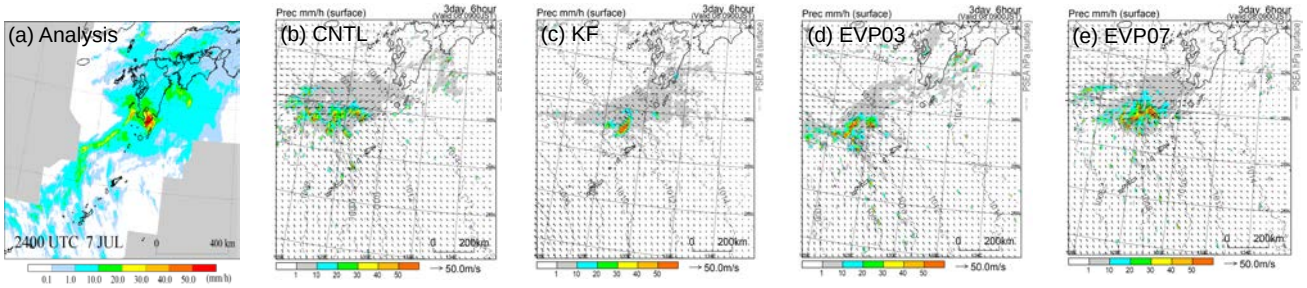

Figure 4 Same as Figure 3 except at 0000 UTC on 8 July.

As is shown in Figure 4a, the precipitation area moved eastward at 0000 UTC on 8 July. Local heavy rainfall included in a broad shield-like precipitation area was observed in the southern Kyusyu region. Results of numerical simulations indicated that the local heavy rainfall and a broad shield-like precipitation were reasonably simulated (Figures 4b-e) particularly in the KF experiment (Figure 4c) although the location quite differed between the analysis and the simulations. In addition, small low pressure analyzed in the weather map (not shown) was simulated in the simulations with the decrease in sea-level pressure of 1.5 hPa in the KF experiment (not shown).

4. Concluding remarks

Nepartak induced distant rainbands that propagated northward toward the Amami Islands. The behavior of the rainbands and resultant shield-like precipitation pattern were reasonably simulated by NHM (not shown) and CPL. This study demonstrated the sensitivity of the precipitation pattern to the cumulus parameterization and cloud physics. However, the location of the shield-like precipitation pattern was not successfully simulated. The effect of the track of simulated typhoon with exact moving speed on the location will be a future subject of this study although the effect was not substantially modified by alternation of the inhibition rate of rain, snow and graupel and the cumulus parameterization. In addition, formation processes of the shield-like precipitation pattern will be clarified by using the results of numerical simulations.

Acknowledgements
This work was supported by JSPS KAKENHI Grant Number JP16H04053 and JP15K05292.

References

Kain, J. S., and J. M. Fritsch (1990). A one-dimensional entraining/detraining plume model and its application in convective parameterization, J. Atmos. Sci., 47, 2784–2802.

Makihara Y (1996). A method for improving radar estimates of precipitation by comparing data from radars and raingauges. J Meteor Soc Japan 74:459-480.

Usui, N., S. Ishizaki, Y. Fujii, H. Tsujino, T. Yasuda and M. Kamachi (2006). Meteorological Research Institute multivariate ocean variational estimation (MOVE) system: Some early results. Advances in Space Research, 37(4), 806-822.

Wada, A., N. Kohno and Y. Kawai (2010). Impact of wave-ocean interaction on Typhoon Hai-Tang in 2005. SOLA, 6A, 13-16.

The 2016 upgrade of the operational NWP at DMI

Xiaohua Yang, xiaohua@dmi.dk, Danish Meteorological Institute (DMI)

During the past years extensive development has been carried out at DMI to extend its operational short range NWP configuration to kilometer-scale resolution with extended area coverage and with mesoscale probabilistic forecasts, aiming to improve forecast of high impact weather. The efforts are now seeing fruits with operational launch of several mesoscale deterministic and probabilistic forecast systems during late 2016 and early 2017. While these new configurations are mainly based on the nonhydrostatic mesoscale HARMONIE-AROME models (Bengtsson et al 2017) with release 40h1.1, numerous local adaptations and extensions have been implemented, especially with many innovations featured in the mesoscale COMEPS (COntinuous Mesoscale EPS) system.

Operational model domains. The new operational setups, NEA, IGA and COMEPS are all constructed at 2.5 km grid resolution and on spatially rather extensive domains. As illustrated in Figure 1, the model domain of NEA covers North Europe including Faroe Islands. NEA (Yang et al 2017a) is a deterministic suite with a 1280x1080x65 mesh, runs 54-h forecast 8 times a day with 3DVAR data assimilation using numerous observation data including satellite radiance, AMV, radio occultation bending angle. IGA (Yang et al 2017b) is a deterministic model covering Iceland and South Greenland with a 1000x800x65 mesh, offering 54h forecast 4 times a day. Finally, COMEPS is a 24-member time-lagged probabilistic forecast system with capability to produce mesoscale ensemble forecast for regions around Denmark, on a grid-mesh of 800x600x65 (Yang et al 2017c).

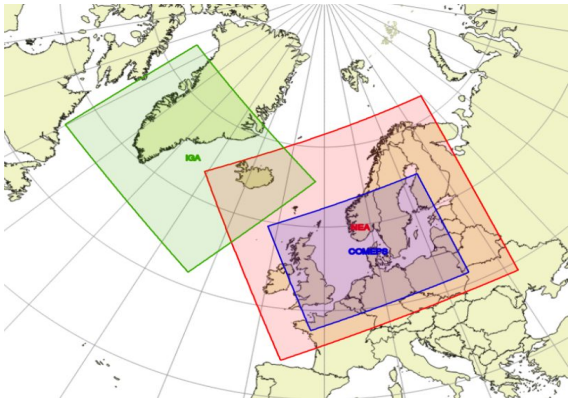

Figure 1: Operational weather forecast suites at DMI with 2.5 km grid spacing. The setup covers North Europe including Faroe Islands (domain NEA, in red), south Greenland and Iceland (domain IGA, in green), and Denmark(with COMEPS EPS, in blue) .

IGA configuration is a joint development between DMI and Icelandic Meteorological Office (IMO) in connection with IMO's hosting of the High Performance Computer (HPC) facility at its headquarter in Reykjavik. IGA brings forward unprecedented high resolution mesoscale forecast capability for Iceland and South Greenland, a region characterised by complex surfaces of high plateaus with glaciers, steep coastal orography, and associated, frequent occurrence of storms and extreme temperature. Significant efforts have been devoted to upgrade and evaluation of database for elevation over Greenland and Iceland, as well as information on glacier extent, soil characteristics, vegetation fractions, albedo and roughness as included in the physiographic database. From observation verification, operational IGA has shown advantages in forecast quality of wind, temperature and precipitation in comparison to other available operational forecasts run at coarser

resolution, especially in detection of storms affecting coastal area. Due to an extensive domain coverage, IGA has also been seen to improve forecast of convective precipitation in west of Iceland associated with cold air outbreak, which has been difficult to capture for models with insufficient domain coverage (Yang et al, 2017b).

Construction of COMEPS, a time-lagged mesoscale EPS system with rapid update. For mesoscale EPS forecast system, it is highly desirable to maintain high resolution with adequate spread, good probabilistic forecast skills, with timely delivery and frequent update. Often, many of these virtues are unfortunately associated with high computational cost and hence difficult to achieve. To address such challenges several innovative features have been implemented in constructions of the new operational mesoscale EPS, COMEPS, at DMI. These include use of time lagging method, perturbation with multi-model, multi-physics, and configuration of data assimilation cycling on overlapping windows. The basic design of COMEPS data flow is that, first, rapid refresh data assimilation is performed each hour using latest available observation including synoptic, radar and satellite radiances. With hourly analysis as control, 4 perturbed forecasts are followed. This is repeated each hour around clock. As result, at any given hour of day, a forecast ensemble can be assembled in time lagged mode using all available perturbed forecasts launched during past 6 hour, resulting 4 member/hour x 6 hour = 24 member COMEPS ensemble. Obviously, in comparison to an EPS with conventional construction, a system constructed with COMEPS approach has advantages in terms of an increased temporal spread, frequent update using latest observations, and a more balanced, evenly distributed HPC load.

At present, COMEPS is a two model ensemble using both HARMONIE and HIRLAM forecast systems. Apart from obtaining spread through time lagging and multi-model approaches, COMEPS also utilises several perturbation techniques to enhance representation of uncertainties, such as use of Scaled LAgged Forecasting (SLAF) for lateral boundary perturbation, use of alternative option mix in physical parameterisation. Operational ECMWF forecast is used as lateral boundary condition via SLAF approach. Another novel configuration feature in COMEPS is the data assimilation cycling, which consists of three parallel sets of data assimilation cycles over overlapping time windows, providing additional opportunity to construct perturbation in initial condition. Radar reflectivity from 10 European countries radar network are assimilated.

Acknowledgements: The work reported in this review is result of collective efforts by colleagues at the research department of DMI.

References

Bengtsson, L., Andrae, U., Aspelien, T., Batrak, Y., Calvo, J., de Rooy, W., Gleeson, E., Sass, B. H., Homleid, M., Hortal, M, Ivarsson, K.-I., Lenderink, G., Niemelä, S., Nielsen, K. P., Onvlee, J., Rontu, L., Samuelsson, P., Santos Muñoz, D., Subias, A., Tijm, S., Toll, V., Yang, X., Køltzow, M. Ø., 2017: The HARMONIE-AROME model configuration in the ALADIN-HIRLAM NWP system, MWR, Vol 145, Nr 5.

Yang, X., B. S. Andersen, M. Dahlbom, B. H. Sass, S. Zhuang, B. Amstrup, C. Petersen, K. P. Nielsen, N. W. Nielsen, A. Mahura, 2017a: NEA, Operational implementation of HARMONIE 40h1.1 at DMI, Joint ALADIN-HIRLAM Newsletter 8, 2017.

Yang, X., B. Palmason, B. S. Andersen, B. H. Sass, B. Amstrup, M. Dahlbom, C. Petersen, K. P. Nielsen, R. Mottram, N. W. Nielsen, A. Mahura, S. Thorsteinsson, N. Nawri and G. N. Petersen, 2017b: IGA, Joint Operational HARMONIE by DMI and IMO. Joint ALADIN-HIRLAM Newsletter 8, 2017.

Yang, X., H. Feddersen, B. H. Sass, and K. Sattler, 2017c: Construction of a continuous mesoscale EPS with time lagging and assimilation on overlapping windows. Joint ALADIN-HIRLAM Newsletter 8, 2017.